Table 2: Daily air pollutant levels and weather information on ADS days and non-ADS days in 2012 and 2013.

(a)

Measurement	ADS days		
	April 23 and 24, 2012	March 8 to 10, 2013	March 19 and 20, 2013
Daily average temperature, °C	17.6 ± 1.1	13.6 ± 3.8	12.4 ± 1.4
Daily maximum temperature, °C	23.3 ± 3.0	20.4 ± 0.9	18.6 ± 0.0
Daily minimum temperature, °C	13.1 ± 0.7	8.0 ± 5.8	7.9 ± 4.5
Daily average relative humidity, %	70.0 ± 5.7	64.7 ± 7.6	79.5 ± 3.5
Daily minimum relative humidity, %	48.0 ± 12.7	29.3 ± 10.7	52.0 ± 0.0
Daily average atmospheric pressure, hPa	1010.8 ± 1.0	1008.6 ± 3.1	1007.4 ± 3.0
Daily average mineral dust particles, km^{-1}	0.046 ± 0.006	0.084 ± 0.077	0.075 ± 0.001
Daily average nonmineral dust particles, km^{-1}	0.148 ± 0.097	0.138 ± 0.050	0.097 ± 0.001
Daily average SPM, $\mu g/m^3$	39.5 ± 2.1	44.3 ± 19.0	32.5 ± 5.0
Daily average $PM_{2.5}$, $\mu g/m^3$	17.2 ± 1.3	37.3 ± 16.7	37.8 ± 4.5
Daily average SO_2, ppb	1.3 ± 0.6	2.0 ± 1.1	1.9 ± 1.3
Daily average NO_2, ppb	1.5 ± 0.4	3.4 ± 1.8	3.6 ± 0.6
Daily average O_x, ppb	55.9 ± 5.7	63.1 ± 10.5	49.4 ± 5.3

(b)

Measurement	Non-ADS days	
	2012	2013
Daily average temperature, °C	15.7 ± 3.5	13.2 ± 5.0
Daily maximum temperature, °C	20.9 ± 4.5	18.7 ± 5.7
Daily minimum temperature, °C	10.9 ± 4.0	8.1 ± 5.0
Daily average relative humidity, %	70.4 ± 9.3	69.8 ± 9.8
Daily minimum relative humidity, %	44.9 ± 15.4	42.8 ± 13.6
Daily average atmospheric pressure, hPa	1010.0 ± 5.7	1011.3 ± 5.9
Daily average mineral dust particles, km^{-1}	0.016 ± 0.010	0.024 ± 0.017
Daily average non-mineral dust particles, km^{-1}	0.042 ± 0.037	0.073 ± 0.049
Daily average SPM, $\mu g/m^3$	17.7 ± 10.1	17.8 ± 8.9
Daily average $PM_{2.5}$, $\mu g/m^3$	10.3 ± 5.4	17.5 ± 7.3
Daily average SO_2, ppb	0.9 ± 0.6	1.0 ± 0.8
Daily average NO_2, ppb	2.6 ± 1.2	2.75 ± 1.2
Daily average O_x, ppb	50.0 ± 7.5	50.2 ± 8.4

Data are presented as the mean ± S.D., Non-ADS days were all other days except for ADS days from April 1 to May 31, 2012, and March 1 to May 31, 2013.

on day 0, −5.49 L/min (−8.14 to −2.85) on day 1, −3.15 L/min (−5.54 to −0.75) on day 2, and −0.72 L/min (−3.03 to 1.59) on day 3 after ADS. A significant decrease in PEF persisted for 2 days after ADS exposure in 2012. In 2013, the changes in PEF were −2.33 L/min (−5.09 to 0.44) on day 0, −2.72 L/min (−4.80 to −0.64) on day 1, −2.26 L/min (−3.98 to −0.53) on day 2, and −3.04 L/min (−4.68 to −1.40) on day 3 after ADS. A significant decrease in PEF continued from days 1 to 3 after ADS exposure. On days 0 and 1, the decrease in PEF after exposure to ADS in 2012 was significantly higher than that in 2013. In addition, the 2012 and 2013 forest plots indicate clear differences. Significant differences were observed in PEF on days 0 and 1, and the decrement of PEF in 2012 was higher than that in 2013. In a two-pollutant model adjusted for SPM, $PM_{2.5}$, SO_2, NO_2, and O_x, an ADS event in 2012 alone was significantly associated with a decrease of PEF (Table 3). In contrast, in 2013, a similar model gave no significant relationship between ADS events and PEF in children.

3.4. IL-8 Transcriptional Activity and IL-8 Secretion in THP-G8 Cells. In THP-G8 cells stimulated for 5 h with various LPS concentrations, nSLO-LA (a measure of IL-8 transcriptional activity) reached a plateau at 100 ng/mL LPS (Figure 4(a)). Maximum induction of nSLO-LA by LPS (100 ng/mL) occurred between 4 and 6 h (Figure 4(b)). Based on these results, we subsequently used stimulation for 5 h to investigate the effect of ADS airborne particles on IL-8 transcriptional activity. The concentrations of IL-8 in supernatants of THP-G8 cells stimulated with vehicle, LPS (n = 6, 1 ng/mL), and LPS (n = 6, 100 ng/mL) were 1.2 ± 0.2, 26.6 ± 6.2, and 77.4 ± 10.9 μg/mL, respectively (Figure 4(c)). This increase in IL-8 secretion is in agreement with the augmentation of nSLO in THP-G8 cells.

The pH values of ADS airborne particles (1 mg/mL) collected on April 23 and 24, 2012; March 8 to 10, 2013; and March 19 and 20, 2013 were 7.9, 7.6, and 7.6, respectively. The nSLO-LA values (IL-8 transcriptional activity) of THP-G8

Table 3: Estimated effects of ADS events on PEF in two-pollutant model after adjustment for SPM, $PM_{2.5}$, NO_2, O_x, and SO_2.

Year	Adjustment	Change in PEF	95% CI	P value
2012 and 2013	Adjusted for SPM	−3.00	−5.31, −0.68	0.011
	Adjusted for $PM_{2.5}$	−3.60	−5.94, −1.27	0.002
	Adjusted for SO_2	−2.14	−4.43, 0.15	0.059
	Adjusted for O_x	−3.49	−5.70, −1.28	0.002
	Adjusted for NO_2	−4.20	−6.37, −2.03	0.001
2012	Adjusted for SPM	−6.04	−9.44, −2.64	0.001
	Adjusted for $PM_{2.5}$	−6.48	−9.78, −3.18	0.001
	Adjusted for SO_2	−7.41	−10.69, −4.13	0.001
	Adjusted for O_x	−3.93	−7.25, −0.62	0.019
	Adjusted for NO_2	−10.04	−13.42, −6.67	0.001
2013	Adjusted for SPM	−1.57	−4.56, 1.43	0.306
	Adjusted for $PM_{2.5}$	−1.97	−5.10, 1.15	0.216
	Adjusted for SO_2	−2.19	−5.02, 0.63	0.128
	Adjusted for O_x	0.19	−2.79, 3.18	0.900
	Adjusted for NO_2	−2.45	−4.38, 1.49	0.085

Calculated for an interquartile by ADS and adjusted for individual characteristics (age, gender, height, weight, and presence of asthma, allergic rhinitis, allergic conjunctivitis, atopic dermatitis, and food allergies) and meteorological variables (temperature, humidity, and atmospheric pressure).
ADS: Asian dust storm, PEF: peak expiratory flow, SPM ($\mu g/m^3$): suspended particle matter, $PM_{2.5}$ ($\mu g/m^3$): particulate matter smaller than 2.5 μm in diameter, NO_2 (ppb): nitrogen dioxide, O_x (ppb): photochemical oxidants, SO_2 (ppb): sulfur dioxide, and CI: confidence interval.

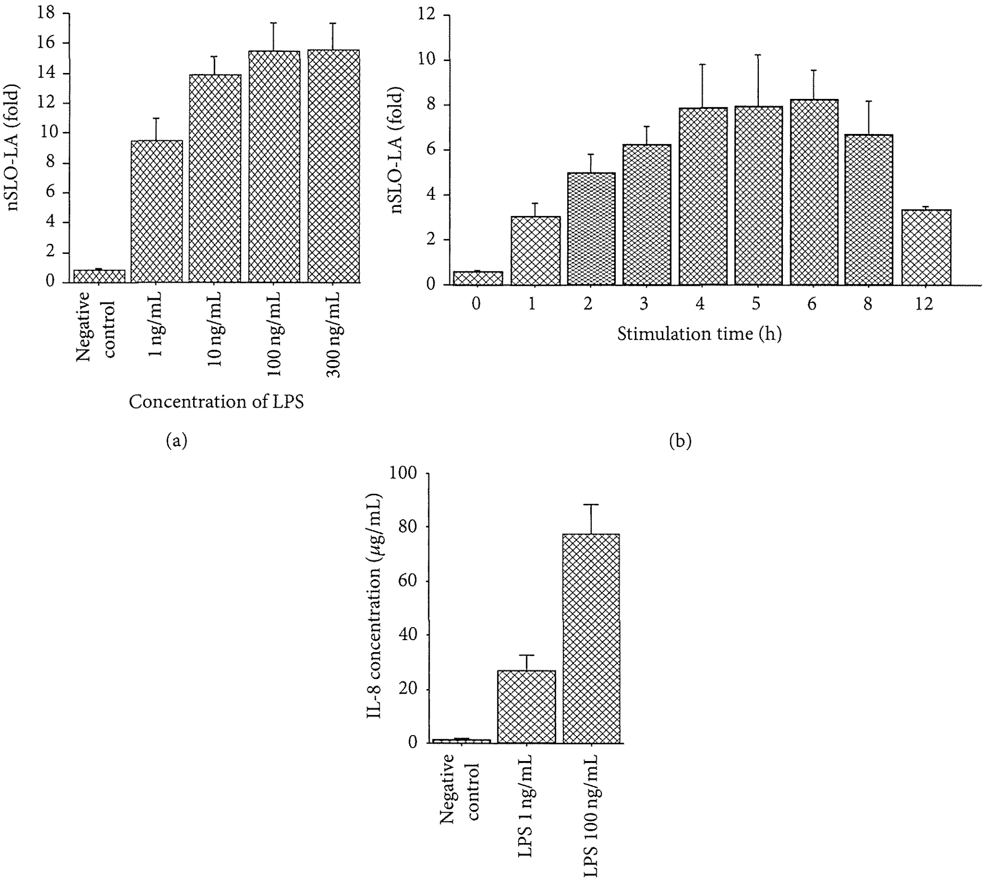

(a)

(b)

(c)

Figure 4: (a) IL-8 transcriptional activity in THP-G8 cells stimulated with LPS at various concentrations ($n = 6$) for 5 h. IL-8 transcriptional activity is based on normalized SLO luciferase activity (nSLO-LA), which was calculated as SLO-LA divided by SLR-LA. The fold induction of nSLO-LA was calculated as the nSLO-LA of treated cells divided by that of untreated cells [18]. (b) IL-8 transcriptional activity in THP-G8 cells stimulated with 100 ng/mL LPS ($n = 6$) for various time periods. (c) Concentrations of IL-8 in supernatants of a stable THP-1-derived IL-8 reporter cell line stimulated with solvent only (negative control), LPS ($n = 6$, 1 ng/mL), and LPS ($n = 6$, 100 ng/mL). The IL-8 concentration was measured using an ELISA kit. Samples were run in triplicate. The assay range was 31.2 to 2000 pg/mL.

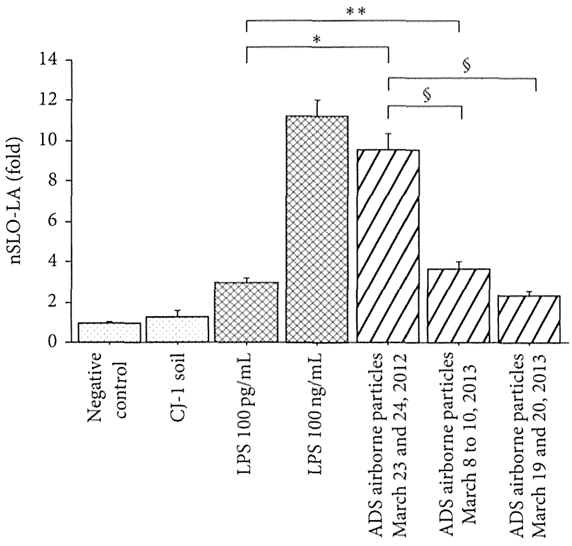

$^{*}P < 0.01$ for the comparison with LPS at 100 pg/mL

$^{**}P < 0.02$ for the comparison with LPS at 100 pg/mL

$^{\S}P < 0.01$ for the comparison with ADS airborne particles in April 23 and 24, 2012

FIGURE 5: IL-8 transcriptional activity measured using an IL-8 luciferase assay in a stable THP-1-derived IL-8 reporter cell line. Cells were treated with solvent only ($n = 6$, negative control), LPS ($n = 6$, 100 pg/mL, positive control), LPS ($n = 6$, 100 ng/mL, positive control), and ADS airborne particles collected on April 23 and 24, 2012 ($n = 6$, 1 mg/mL), March 8 to 10, 2013 ($n = 6$, 1 mg/mL), and March 19 and 20, 2013 ($n = 6$, 1 mg/mL). $^{*}P < 0.01$ versus LPS at 100 pg/mL, $^{**}P < 0.02$ versus LPS at 100 pg/mL, and $^{\S}P < 0.01$ versus ADS airborne particles from April 23 to April 24, 2012.

cells (Figure 5) changed by 0.95 ± 0.09-fold (vehicle, $n = 6$), 2.87 ± 0.28-fold (LPS, $n = 6$, 100 pg/mL), 11.21 ± 0.28-fold (LPS, $n = 6$, 100 ng/mL), 9.56 ± 0.80-fold (ADS particles from April 23 to 24, 2012, $n = 6$, 1 mg/mL), 3.65 ± 0.36-fold (ADS particles from March 8 to 10, 2013, $n = 6$, 1 mg/mL), and 2.33 ± 0.24-fold (ADS particles from March 19 to 20, 2013, $n = 6$, 1 mg/mL).

The pH value of CJ-1 soil was constant at 8.4 for each event. The pH values of ADS airborne particles (1 mg/mL) collected on April 23 and 24, 2012; March 8 to 10, 2013; and March 19 and 20, 2013 were 7.9, 7.6, and 7.6, respectively. THP-G8 cells were stimulated with CJ-1 soil after adjusting the pH of the soil to 7.8 with 0.1 N sodium hydroxide. The nSLO-LA values (IL-8 transcriptional activity) of THP-G8 cells (Figure 5) changed by 0.95 ± 0.09-fold (vehicle, $n = 6$), 1.48 ± 0.27-fold (CJ-1 soil, $n = 6$, 1 mg/mL), 2.87 ± 0.28-fold (LPS, $n = 6$, 100 pg/mL), 11.21 ± 0.28-fold (LPS, $n = 6$, 100 ng/mL), 9.56 ± 0.80-fold (ADS particles from April 23 to 24, 2012, $n = 6$, 1 mg/mL), 3.65 ± 0.36-fold (ADS particles from March 8 to 10, 2013, $n = 6$, 1 mg/mL), and 2.33 ± 0.24-fold (ADS particles from March 19 to 20, 2013, $n = 6$, 1 mg/mL). nSLO-LA values in THP-G8 cells stimulated by ADS airborne particles differed significantly from those of controls and cells stimulated with 100 pg/mL LPS. nSLO-LA values also differed significantly for each pairwise comparison of airborne particles collected in the three ADS periods.

3.5. Endotoxin Concentration in Airborne Particles Collected on ADS Days.

The endotoxin levels in ADS airborne particles (1 mg/mL) collected on April 23 and 24, 2012; March 8 to 10, 2013; and March 19 and 20, 2013 were 0.19, 0.08, and 0.07 EU/mL, respectively. These values were all lower than the level of 0.89 EU/mL found in 100 pg/mL LPS. The endotoxin concentration in 100 ng/mL LPS was out of the range of the assay.

3.6. Concentration of Metal Elements in CJ-1 Soil and Airborne Particles Collected on ADS Days.

The concentrations of metal elements in CJ-1 soil and ADS airborne particles collected on April 23 and 24, 2012; March 8 to 10, 2013; and March 19 and 20, 2013 are shown in Table 4.

4. Discussion

To investigate the effect of ADS on pulmonary function, we monitored daily PEF in school children from April to May 2012 and March to May 2013 and found a significant correlation between exposure to an ADS and pulmonary function. The 2012 survey alone also showed this relationship. When differences in PEF between the 2012 and 2013 results were evaluated, the same relationship of PEF with ADS events was not found in 2013, despite the study being conducted in the same children. The decline of PEF upon ADS exposure in 2012 was also significantly higher than that in 2013, and IL-8 transcriptional activity in THP-G8 cells induced by ADS airborne particles collected in 2012 was also significantly higher than that induced by ADS airborne particles collected in 2013. These results suggest that the effect of ADS on pulmonary function in children is associated with enhanced airway inflammation mediated by elevation of IL-8.

Desert sand can reduce pulmonary function in patients with asthma after exposure at a level of PM_{10} ranging from 1500 to 2000 $\mu g/m^3$/hour [25]. This level of PM_{10} is 10 to 20 times higher than that during an ADS event in Japan. In the current study, the level of mineral dust particles on ADS events on March 8 to 10, 2013, and March 19 and 20, 2013 was about twice as high as that in 2012. However, the decrease of PEF after exposure to ADS in 2012 was higher than that in 2013. These results suggest that the decline in pulmonary function of school children during an ADS event has little connection to mineral dust particles (sand dust particles). Nonmineral dust particles were similar on ADS events in 2012 and 2013. ADS events in 2012 had higher counts of air pollution aerosols than those in 2013. Based on Onishi's criteria [4], the ADS event in 2012 can be classified as Type 1 and those in 2013 as type 2. The air pollution aerosols during ADS can be considered a cause of the significant difference in the effect of the ADS on pulmonary function of school children between 2012 and 2013.

The ADS days in 2013 were defined as moderate, while, on April 23 and 24, 2012, the mean daily average concentration of mineral dust particles was 0.046 ± 0.006 km^{-1} in Matsue

Table 4: Concentration of metal elements in CJ-1 soil and airborne particles collected on ADS days.

Metals (μg/mg)	CJ-1 soil	ADS airborne particles in April 23 and 24, 2012	ADS airborne particles in March 8 to 10, 2013	ADS airborne particles in March 19 and 20, 2013
Al	68.00	28.80	22.40	14.80
As	ND	ND	ND	ND
Ba	0.44	0.12	0.18	0.10
Ca	68.00	29.60	44.00	31.20
Cd	ND	ND	ND	ND
Co	0.01	ND	ND	ND
Cr	0.05	ND	ND	ND
Cu	0.03	0.12	ND	0.07
Fe	26.00	22.00	20.80	14.40
Hg	ND	ND	ND	ND
K	0.19	0.38	0.33	0.30
La	0.03	ND	ND	ND
Mg	18.00	14.00	16.80	14.40
Mn	0.70	0.52	0.56	0.40
Na	0.44	33.60	56.00	64.00
Ni	0.03	0.14	0.15	0.11
P	0.68	ND	ND	ND
Pb	0.02	0.06	0.12	0.06
Si	260.00	140.00	108.00	72.00
Sr	0.26	0.16	0.22	0.16
Ti	2.40	0.96	0.92	0.52
Zn	0.07	0.52	0.64	0.60

ADS: Asian dust storm, CJ-1 soil: soil from the China Loess Plateau, the original ADS soil in the Tengger Desert and Huining located in Gansu Province, and ND: not detected.

City. These values are lower than the thresholds defined in previous studies [9, 21]. However, the daily average level of mineral dust particles on ADS days was higher than that on non-ADS days, as required for definition of an ADS day in the Japan Meteorological Agency criteria used in this study.

Many studies have shown that children are susceptible to air pollution such as NO_2, O_x, and SO_2 [18, 26]. Therefore, we used a linear mixed model and a two-pollutant model to adjust for the effects of NO_2, O_x, and SO_2 on pulmonary function. In both models, ADS in 2012 remained significant after inclusion of NO_2, O_x, and SO_2. However, in the 2013 survey, we were not able to find a significant association with ADS and pulmonary function. These results suggest that airborne particles during ADS decrease pulmonary function irrespective of NO_2, O_x, and SO_2.

IL-8 is a key cytokine in air pollutant-induced airway inflammation [15, 16]. Components that adhered to ADS particles can increase release of IL-6 and IL-8 from airway epithelial cells [27]. We showed that ADS airborne particles promote transcriptional activity and production of IL-8 in THP-G8 cells, with a significant increase in IL-8 transcriptional activity in THP-G8 cells treated with ADS airborne particles compared to those treated with original ADS soil (CJ-1 soil). Additionally, we measured the difference in production of IL-8 by particles collected during each ADS event. The IL-8 transcriptional activity of ADS airborne particles collected in 2012 was significantly higher than that for particles collected in 2013. This difference in production of IL-8 by ADS airborne particles may account for the different effects on pulmonary function in school children in 2012 and 2013.

The production of IL-8 induced by ADS airborne particles in 2012 had a significant difference compared to 2013. However, there was no difference between the two ADS airborne particles in 2013. The ADS events in 2013 had happened close together, and we suspect that the route and composition of the ADS airborne particles in the two events were similar. In fact, when we analyzed the effect on PEF between two ADS events in 2013 separately, the decreases in PEF after exposure to ADS were −4.1 L/min (95% CI, −10.6 to 2.4, $P = 0.21$) in March 8 to 10 and −3.3 L/min (95% CI, −10.8 to 4.1, $P = 0.37$) in March 19 and 20. In both ADS events in 2013, there was not a significant decrease of the effects on PEF. Therefore, we presented the combined results in the main analysis. The differences in the substances and the levels of those substances attached to desert sand dusts depend on the route along which desert sand dusts pass and may play an important role in the effect of ADS on pulmonary function in children.

According to the analysis of the concentrations of metal elements, ADS airborne particles in 2012 had more Al, Cu, Fe, K, and Ti compared to those on March 8 to 10 and March 19 and 20, 2013. The amounts of Al, Fe, and Ti in ADS airborne particles in 2012 were lower than CJ-1. Cu and K may play a causative role in the difference of production of IL-8 induced by ADS airborne particles. However, Kumar et al. indicated that Cu was not a cause of the production of CXCL1 (a mouse functional homologue of IL-8) and IL-6 induced by ambient and traffic-derived particulate matter, but it did indicate that Fe content of airborne particulate matter may be more important in mouse airway epithelial injury [28]. Metal components attached to ADS airborne particles may be one of the causes of the difference between 2012 and 2013, but further study is needed to determine a role of metal components attached to ADS on the effect of production of proinflammatory cytokines.

Ogino et al. found that some proteins contained in ambient particulate matter are important environmental factors that aggravate airway hyperresponsiveness and airway inflammation in mice [29]. An ADS contains different amounts of β-glucan, which can induce airway inflammation [30, 31]. Thus, in addition to chemical substances, anthropogenic metal components, and sulfate, some proteins and β-glucan attached to ADS airborne particles may play important roles in the reduction of pulmonary function during ADS events.

Inhaled LPS is associated with airway neutrophil inflammation in patients with asthma and in healthy subjects [32–34]. Our results show that ADS airborne particles contain endotoxin, and the endotoxin concentration of ADS airborne particle was lower than that in LPS at 100 pg/mL. However, the IL-8 transcriptional activity induced by ADS airborne particle collected on April 23 and 24, 2012 and March 8 to 10, 2013 was significantly higher than that induced by LPS at 100 pg/mL. Endotoxin may augment IL-8 transcriptional activity in THP-G8 cells, in addition to other substances on ADS airborne particles that may induce IL-8.

Park et al. [10] and Yoo et al. [35] found a relationship between ADS events and PEF in Korean children with asthma, while Hong et al. did not find a significant relationship between ADS events and PEF in children without asthma [36]. Patients with allergic diseases may also be more sensitive to air pollution [37–39]. Therefore, in this study, we analyzed the data after adjustment for allergic diseases. This analysis showed that there was a significant decrease of PEF on ADS days in 2012 compared to 2013, regardless of the presence of allergic diseases. However, the number of subjects with each disease was too small to investigate the association of PEF with ADS. Further studies are needed to define the relationship between ADS and PEF in children with allergic diseases.

In this study, children recorded their PEF value after arriving at school but did not record their PEF value on weekends and public holidays. The ADS days March 9, 10, and 20, 2013 lacked PEF data because they were holidays. However, this intermittent missing data is statistically independent of the ADS events. Thus, it would not cause any serious bias in the results. Although it would raise a reduction of statistical power, the significant associations were still observed in the primary analyses.

There are several limitations in the study. First, we did not investigate diseases other than asthma, allergic rhinitis, allergic conjunctivitis, atopic dermatitis, and food allergies. Second, we were unable to diagnose asthma based on airway hyperresponsiveness to methacholine and reversible airflow limitation. In this study, some children were considered to have asthma, when in fact their wheezing may have been caused by respiratory tract infection or other diseases. However, wheezing caused by respiratory tract infection and other diseases is more common in children under 6 years old, and that is younger than those in our study [40]. Additionally, it is difficult to distinguish asthma and reactive airway disease based on the present diagnostic criteria. Third, we were unable to measure the individual amount of exposure to ADS. Fourth, we did not analyze the composition of the ADS airborne particles. Therefore, this study was not able to investigate which components of ADS airborne particles played important roles in reduction of pulmonary function during the ADS and which components induce IL-8. Further studies are needed to define these components.

5. Conclusion

We conclude that the effect of exposure to ADS on pulmonary function in school children differed among ADS events, and that enhancement of IL-8 transcriptional activity also differed among ADS airborne particles collected during the respective events. These findings suggest that substances attached to ADS airborne particles exacerbate pulmonary function of school children. Further studies are needed to identify the substances attached to the ADS airborne particles that play key roles in exacerbation of pulmonary function.

Conflict of Interests

The authors declare that there is no conflict of interests regarding the publication of this paper.

Acknowledgments

The authors thank Atsushi Shimizu and Nobuo Sugimoto in the National Institute for Environmental Studies for providing them with LIDAR data. The study was supported by the Environmental Research and Technology Development Fund (5C-1154 and 5-1453) of the Japanese Ministry of the Environment. The sponsors had no role in the study design; in the collection, analysis, and interpretation of data; in the writing of the report; or in the decision to submit the paper for publication.

References

[1] T. Y. Tanaka and M. Chiba, "A numerical study of the contributions of dust source regions to the global dust budget," *Global and Planetary Change*, vol. 52, no. 1–4, pp. 88–104, 2006.

[2] J. C. Choi, M. Lee, Y. Chun, J. Kim, and S. Oh, "Chemical composition and source signature of spring aerosol in Seoul, Korea," *Journal of Geophysical Research D: Atmospheres*, vol. 106, no. 16, pp. 18067–18074, 2001.

[3] Y.-J. Han, T. M. Holsen, P. K. Hopke, J.-P. Cheong, H. Kim, and S.-M. Yi, "Identification of source locations for atmospheric dry deposition of heavy metals during yellow-sand events in Seoul, Korea in 1998 using hybrid receptor models," *Atmospheric Environment*, vol. 38, no. 31, pp. 5353–5361, 2004.

[4] K. Onishi, Y. Kurosaki, S. Otani, A. Yoshida, N. Sugimoto, and Y. Kurozawa, "Atmospheric transport route determines components of Asian dust and health effects in Japan," *Atmospheric Environment*, vol. 49, pp. 94–102, 2012.

[5] Y.-S. Chen, P.-C. Sheen, E.-R. Chen, Y.-K. Liu, T.-N. Wu, and C.-Y. Yang, "Effects of Asian dust storm events on daily mortality in Taipei, Taiwan," *Environmental Research*, vol. 95, no. 2, pp. 151–155, 2004.

[6] H.-J. Kwon, S.-H. Cho, Y. Chun, F. Lagarde, and G. Pershagen, "Effects of the Asian dust events on daily mortality in Seoul, Korea," *Environmental Research*, vol. 90, no. 1, pp. 1–5, 2002.

[7] L. W. Lai and W. L. Cheng, "The impact of air quality on respiratory admissions during Asian dust storm periods," *International Journal of Environmental Health Research*, vol. 18, no. 6, pp. 429–450, 2008.

[8] C.-Y. Yang, Y.-S. Chen, H.-F. Chiu, and W. B. Goggins, "Effects of Asian dust storm events on daily stroke admissions in Taipei, Taiwan," *Environmental Research*, vol. 99, no. 1, pp. 79–84, 2005.

[9] K. T. Kanatani, I. Ito, W. K. Al-Delaimy et al., "Desert dust exposure is associated with increased risk of asthma hospitalization in children," *The American Journal of Respiratory and Critical Care Medicine*, vol. 182, no. 12, pp. 1475–1481, 2010.

[10] J. W. Park, Y. H. Lim, S. Y. Kyung et al., "Effects of ambient particulate matter on peak expiratory flow rates and respiratory symptoms of asthmatics during Asian dust periods in Korea," *Respirology*, vol. 10, no. 4, pp. 470–476, 2005.

[11] C. Y. Yang, S. S. Tsai, C. C. Chang, and S. C. Ho, "Effects of Asian dust storm events on daily admissions for asthma in Taipei, Taiwan," *Inhalation Toxicology*, vol. 17, no. 14, pp. 817–821, 2005.

[12] M. L. Bell, J. K. Levy, and Z. Lin, "The effect of sandstorms and air pollution on cause-specific hospital admissions in Taipei, Taiwan," *Occupational and Environmental Medicine*, vol. 65, no. 2, pp. 104–111, 2008.

[13] M. Watanabe, J. Kurai, T. Igishi et al., "Influence of Asian desert dust on lower respiratory tract symptoms in patients with asthma over 4 years," *Yonago Acta Medica*, vol. 55, no. 2, pp. 41–48, 2012.

[14] M. P. Sierra-Vargas, A. M. Guzman-Grenfell, S. Blanco-Jimenez et al., "Airborne particulate matter $PM_{2.5}$ from Mexico City affects the generation of reactive oxygen species by blood neutrophils from asthmatics: an in vitro approach," *Journal of Occupational Medicine and Toxicology*, vol. 4, article 17, 2009.

[15] S. T. Holgate, T. Sandström, A. J. Frew et al., "Health effects of acute exposure to air pollution. Part I: healthy and asthmatic subjects exposed to diesel exhaust," *Research Report (Health Effects Institute)*, no. 112, pp. 1–30, 51–67, 2003.

[16] J. Bellido-Cassado, V. Plaza, M. Perpina et al., "Inflammatory response of rapid onset asthma exacerbation," *Archivos de Bronconeumología*, vol. 46, pp. 587–593, 2010.

[17] M. Watanabe, J. Kurai, K. Tomita et al., "Effects on asthma and induction of interleukin-8 caused by Asian dust particles collected in western Japan," *Journal of Asthma*, vol. 51, no. 6, pp. 595–602, 2014.

[18] D. J. Ward and J. G. Ayres, "Particulate air pollution and panel studies in children: a systematic review," *Occupational and Environmental Medicine*, vol. 61, no. 4, article e13, 2004.

[19] N. Sugimoto and C. H. Lee, "Characteristics of dust aerosols inferred from lidar depolarization measurements at two wavelengths," *Applied Optics*, vol. 45, no. 28, pp. 7468–7474, 2006.

[20] M. Sugimoto, I. Matsui, and A. Shimizu, "Lidar network observations of tropospheric aerosols," in *Lidar Remote Sensing for Environmental Monitoring IX*, vol. 71530 of *Proceedings of SPIE*, 2008.

[21] K. Ueda, A. Shimizu, H. Nitta, and K. Inoue, "Long-range transported Asian Dust and emergency ambulance dispatches," *Inhalation Toxicology*, vol. 24, no. 12, pp. 858–867, 2012.

[22] T. Takahashi, Y. Kimura, R. Saito et al., "An *in vitro* test to screen skin sensitizers using a stable THP-1-derived IL-8 reporter cell line, THP-G8," *Toxicological Sciences*, vol. 124, no. 2, pp. 359–369, 2011.

[23] N. M. Laird and J. H. Ware, "Random-effects models for longitudinal data," *Biometrics*, vol. 38, no. 4, pp. 963–974, 1982.

[24] G. Verbeke and G. Molenberghs, *Linear Mixed Models for Longitudinal Data*, Springer, New York, NY, USA, 2nd edition, 2009.

[25] P. Gupta, S. Singh, S. Kumar, M. Choudhary, and V. Singh, "Effect of dust aerosol in patients with asthma," *Journal of Asthma*, vol. 49, no. 2, pp. 134–138, 2012.

[26] B. Linares, J. M. Guizar, N. Amador et al., "Impact of air pollution on pulmonary function and respiratory symptoms in children. Longitudinal repeated-measures study," *BMC Pulmonary Medicine*, vol. 10, article 62, 2010.

[27] A. Honda, Y. Matsuda, R. Murayama et al., "Effects of Asian sand dust particles on the respiratory and immune system," *Journal of Applied Toxicology*, vol. 34, no. 3, pp. 250–257, 2014.

[28] R. K. Kumar, A. M. Shadie, M. P. Bucknall et al., "Differential injurious effects of ambient and traffic-derived particulate matter on airway epithelial cells," *Respirology*, 2014.

[29] K. Ogino, N. Takahashi, M. Kubo, A. Takeuchi, M. Nakagiri, and Y. Fujikura, "Inflammatory airway responses by nasal inoculation of suspended particulate matter in NC/Nga mice," *Environmental Toxicology*, vol. 29, no. 6, pp. 642–654, 2014.

[30] M. He, T. Ichinose, Y. Song et al., "Effects of two Asian sand dusts transported from the dust source regions of Inner Mongolia and northeast China on murine lung eosinophilia," *Toxicology and Applied Pharmacology*, vol. 272, no. 3, pp. 647–655, 2013.

[31] T. Ichinose, S. Yoshida, K. Hiyoshi et al., "The effects of microbial materials adhered to Asian sand dust on allergic lung inflammation," *Archives of Environmental Contamination and Toxicology*, vol. 55, no. 3, pp. 348–357, 2008.

[32] N. Alexis, M. Eldridge, W. Reed, P. Bromberg, and D. B. Peden, "CD14-dependent airway neutrophil response to inhaled LPS: Role of atopy," *Journal of Allergy and Clinical Immunology*, vol. 107, no. 1, pp. 31–35, 2001.

[33] N. E. Alexis and D. B. Peden, "Inflammatory response of the airway to inhaled endotoxin correlates with body mass index in atopic patients with asthma but not in normal volunteers," *Journal of Allergy and Clinical Immunology*, vol. 117, no. 5, pp. 1185–1186, 2006.

[34] B. Behbod, B. Urch, M. Speck et al., "Endotoxin in concentrated coarse and fine ambient particles induces acute systemic inflammation in controlled human exposures," *Occupational and Environmental Medicine*, vol. 70, no. 11, pp. 761–767, 2013.

[35] Y. Yoo, T. C. Ji, J. Yu, K. K. Do, and Y. K. Young, "Acute effects of Asian dust events on respiratory symptoms and peak expiratory flow in children with mild asthma," *Journal of Korean Medical Science*, vol. 23, no. 1, pp. 66–71, 2008.

[36] Y.-C. Hong, X.-C. Pan, S.-Y. Kim et al., "Asian Dust Storm and pulmonary function of school children in Seoul," *Science of the Total Environment*, vol. 408, no. 4, pp. 754–759, 2010.

[37] R. Shturman-Ellstein, R. J. Zeballos, J. M. Buckley, and J. F. Souhrada, "The beneficial effect of nasal breathing on exercise-induced bronchoconstriction," *American Review of Respiratory Disease*, vol. 118, no. 1, pp. 65–73, 1978.

[38] S. Otani, K. Onishi, H. Mu et al., "The relationship between skin symptoms and allergic reactions to Asian dust," *International Journal of Environmental Research and Public Health*, vol. 9, no. 12, pp. 4606–4614, 2012.

[39] S. Otani, K. Onishi, H. Mu, T. Hosoda, Y. Kurozawa, and M. Ikeguchi, "Associations between subjective symptoms and serum immunoglobulin e levels during asian dust events," *International Journal of Environmental Research and Public Health*, vol. 4, pp. 7636–7641, 2014.

[40] R. T. Stein, C. J. Holberg, W. J. Morgan et al., "Peak flow variability, methacholine responsiveness and atopy as markers for detecting different wheezing phenotypes in childhood," *Thorax*, vol. 52, no. 11, pp. 946–952, 1997.

Anal Bioanal Chem (2014) 406:5735–5742
DOI 10.1007/s00216-014-7981-7

RESEARCH PAPER

Dual-color bioluminescence imaging assay using green- and red-emitting beetle luciferases at subcellular resolution

Mayu Yasunaga · Yoshihiro Nakajima · Yoshihiro Ohmiya

Received: 31 January 2014 / Revised: 9 June 2014 / Accepted: 16 June 2014 / Published online: 12 July 2014

Abstract Bioluminescence imaging is widely used to monitor cellular events, including gene expression in vivo and in vitro. Moreover, recent advances in luciferase technology have made possible imaging at the single-cell level. To improve the bioluminescence imaging system, we have developed a dual-color imaging system in which the green-emitting luciferase from a Brazilian click beetle (Emerald Luc, ELuc) and the red-emitting luciferase from a railroad worm (Stable Luciferase Red, SLR) were used as reporters, which were localized to the peroxisome and the nucleus, respectively. We clearly captured simultaneously the subcellular localization of ELuc in the peroxisome and SLR in the nucleus of a single cell using a high-magnification objective lens with 3-min exposure time without binning using a combination of optical filters. Furthermore, to apply this system to quantitative time-lapse imaging, the activation of nuclear factor triggered by tumor necrosis factor α was measured using nuclear-targeted SLR and peroxisome-targeted ELuc as the test and internal control reporters, respectively. We successfully quantified the kinetics of activation of nuclear factor κB using nuclear-targeted SLR and the transcriptional change of the internal control promoter using peroxisome-targeted ELuc simultaneously in a single cell, and showed that the activation kinetics, including activation rate and amplitude, differed among cells. The results demonstrated that this imaging system can visualize the subcellular localization of reporters and track the expressions of two genes simultaneously at subcellular resolution.

Keywords Dual-color bioluminescence imaging · Luciferase · Nuclear factor κB · Subcellular imaging · Time-lapse imaging

Introduction

Bioluminescent reporters have become an essential tool for studying various aspects of biological functions, including gene expression, posttranscriptional modification, and protein–protein interactions, because the sensitivity and range of the linear response are superior to those of other reporters, including β-galactosidase, chloramphenicol acetyltransferase, and fluorescent proteins [1, 2]. In particular, luciferases are used as sensitive reporters to monitor gene expression noninvasively, quantitatively, and longitudinally in living cells, in explant tissues, and in vivo [3–5].

Recent advances in luciferase technology have made possible the quantitative visualization of gene expression at single-cell resolution by imaging luciferase luminescence in real time using a highly sensitive charged-coupled device (CCD) camera [4–6]. Although fluorescence imaging techniques that use fluorescent proteins (e.g., green fluorescent protein and its derivatives) as probes have contributed immensely to the advancement of cell biology and are used as powerful probes to monitor an extensive array of entities, ranging from single molecules to whole organisms,

---

Published in the topical collection *Analytical Bioluminescence and Chemiluminescence* with guest editors Elisa Michelini and Mara Mirasoli.

Electronic supplementary material The online version of this article (doi:10.1007/s00216-014-7981-7) contains supplementary material, which is available to authorized users.

M. Yasunaga · Y. Nakajima (✉)
Health Research Institute, National Institute of Advanced Industrial Science and Technology (AIST), 2217-14 Hayashi-cho, Takamatsu, Kagawa 761-0395, Japan
e-mail: y-nakajima@aist.go.jp

Y. Ohmiya (✉)
DAILAB, Biomedical Research Institute, National Institute of Advanced Industrial Science and Technology (AIST), Central 6, 1-1-1 Higashi, Tsukuba, Ibaraki 305-8566, Japan
e-mail: y-ohmiya@aist.go.jp

bioluminescence imaging is rapidly emerging as a new and sensitive approach to understanding cell physiology.

The luciferase emits light by oxidizing its substrate, luciferin, in a specific manner [7]. Among the possible luciferase/luciferin reactions, the beetle luciferase and D-luciferin (a benzothiazole) pair is the best probe for the long-term and noninvasive detection of cellular events, because the luminescence generated by the reaction is highly quantitative and has an extremely low background, and D-luciferin is stable and easily permeates cells and tissues [8–10]. Moreover, no external illumination is required to induce bioluminescent reactions. Therefore, the characteristic properties of the beetle luciferase/luciferin reaction allow cellular events to be monitored longitudinally and quantitatively.

Of the luciferases identified to date, the firefly luciferase from *Photinus pyralis* is the most commonly used as a bioluminescent reporter. Although this reporter has been extensively used to monitor multiple cellular events in cell extraction assays, cell-based assays, and in vivo and single-cell imaging [1, 2, 11], the light output of this reporter from living cells is insufficient for analyses at high temporal and/or spatial resolution. In particular, bioluminescence imaging at the subcellular level is difficult because of the insufficient light output of available probes. To overcome this limitation, we have recently developed a brighter green-emitting luciferase (Emerald Luc, ELuc), from Brazilian click beetle, and achieved imaging at the subcellular level with high resolution [12].

Improvements in luciferases and detection systems have enabled us to monitor the expressions of multiple genes simultaneously using luciferases that emit light of different colors [4, 5]. To detect two genes simultaneously, green- and red-emitting beetle luciferases that act on a single D-luciferin substrate are commonly used. Any two or more luciferases that stably emit separable emission spectra can be combined to monitor the expression of multiple genes simultaneously. This system has been widely used for cell extraction assays or real-time monitoring in bacteria [13], yeasts [14], cultured plant tissues [15], cultured mammalian cells [16–25], and explanted tissues [26, 27], as well as for in vivo imaging [28–31]. Furthermore, more recently, we and others have applied the dual-color luciferase system to the time-lapse bioluminescence imaging of a single cell to quantitatively and simultaneously track expressions of clock genes [32] and genes involved in somitogenesis [33, 34] using ELuc and a red-emitting luciferase (Stable Luciferase Red, SLR).

Although the dual-color luciferase system has succeeded in visualizing multiple gene expressions simultaneously at the single-cell level, it has never achieved dual-color imaging at subcellular resolution. To improve the bioluminescence imaging system, we have developed a dual-color bioluminescence imaging system in which peroxisome-targeted ELuc and nuclear-targeted SLR are used as reporters in combination with optical filters. With this system, we have successfully imaged the subcellular localization of the reporters simultaneously with high spatiotemporal resolution, and tracked two gene expressions at subcellular resolution.

Materials and methods

Plasmid construction

To construct a reporter plasmid carrying peroxisome-targeted ELuc, the complementary DNA sequence in which the start codon was replaced by an *Eco*RV site was amplified by polymerase chain reaction using pELuc-test (Toyobo, Osaka, Japan) as the template. The amplified product was ligated into the *Eco*RV/*Xho*I site of pCMV-Tag2B (Stratagene) downstream of the immediate cytomegalovirus (CMV) promoter, which resulted in the pCMV-ELuc (pox) construct. To generate plasmid carrying nuclear-targeted SLR, the complementary DNA sequence in which the peroxisomal targeting signal (Ser-Lys-Leu) at the extreme C-terminus and the stop codon of SLR were replaced by a *Xho*I site was amplified by polymerase chain reaction using pSLR-test (Toyobo) as the template. The amplified fragment was ligated into the *Nco*I/*Xho*I site of pCMV/myc/nuc (Invitrogen, Carlsbad, CA, USA), in which a triple nuclear localization signal from SV40 large T antigen was introduced downstream of the multiple-cloning site, for C-terminal fusion to the SLR, resulting in the pCMV-SLR (nuc) construct. To generate a nuclear factor κB (NF-κB) reporter plasmid, oligonucleotides containing six tandem repeats of the NF-κB response element (NF-κB RE; 5′-CGGA AAGTCCA-3′) were ligated into the *Xho*I/*Bgl*II site of pSLR-HSVtk Control (Toyobo), immediately upstream of the herpes simplex virus thymidine kinase promoter. The SLR gene was replaced by nuclear localization signal fused SLR with the *Nco*I and *Xba*I fragment of pCMV-SLR (nuc) to generate pNFκB-TK-SLR (nuc).

Cell culture and transfection procedures

Mouse NIH3T3 cells (Riken Cell Bank 1862) were grown in Dulbecco's modified Eagle's medium (DMEM; Sigma-Aldrich, St Louis, MO, USA) supplemented with 10 % fetal bovine serum (FBS; ICN Biochemicals, Aurora, OH, USA) in a humidified atmosphere containing 5 % CO_2 at 37 °C. One day before the transfection, the cells were seeded in 35-mm glass-bottom dishes (Iwaki, Tokyo, Japan) at 5×10^5 cells per dish unless otherwise noted. Transfection was performed using Lipofectamine PLUS (Invitrogen) according to the manufacturer's instructions.

Spectral measurements

To measure bioluminescence spectra in living cells, NIH3T3 cells were transfected with 2 μg of pCMV-ELuc (pox) or pCMV-SLR (nuc), and cultured for 1 day. The medium was replaced with DMEM without phenol red (Gibco-BRL, Grand Island, NY, USA) supplemented with 10 % FBS, 25 mM*N*-(2-hydroxyethyl)piperazine-*N*′-ethanesulfonic acid (Hepes)/NaOH (pH 7.0; Sigma-Aldrich), and 200 μM D-luciferin potassium salt (Toyobo). The dish was placed on the sample stage of a spectrophotometer (AB-1850, ATTO, Tokyo, Japan), and spectral measurements were performed noninvasively for 1 min with a slit width of 1 mm.

Bioluminescence imaging

For bioluminescence imaging, NIH3T3 cells were transfected with reporter plasmid, and were seeded in 35-mm glass-bottom dishes (Iwaki) at 5×10^5 cells per dish and incubated for 1 day. The culture medium was replaced with DMEM without phenol red (Gibco) supplemented with 10 % FBS, 25 mM Hepes/NaOH (pH 7.0; Sigma-Aldrich), and 500 μM D-luciferin potassium salt (Toyobo), and was overlaid with 2 ml of mineral oil (Sigma-Aldrich) to prevent evaporation. For tumor necrosis factor α (TNFα) treatment, TNFα (Wako, Tokyo, Japan) at 10 ng/ml was added to the DMEM described earlier. Bioluminescence imaging was performed using a CellGraph (ATTO) luminescence microscope at 37 °C. CCD images were acquired using a ×20 or ×40 objective lens (numerical aperture, 0.9; Nikon, Tokyo, Japan) at 1 × 1 binning of the 512×512 pixel array in the absence or presence of BG39 short-pass (SCHOTT, Duryea, PA, USA) and R62 long-pass (HOYA, Tokyo, Japan) optical filters. Luminescence intensity was quantified using CellGraph Viewer (ATTO) and Metamorph (Universal Imaging, Brandywine, PA, USA).

Real-time measurement of ELuc and SLR luminescence using a luminometer

NIH3T3 cells were seeded in 35-mm dishes (Iwaki) at 5×10^5 cells 1 day before transfection. NIH3T3 cells were cotransfected with 1 μg of reporter plasmid pCMV-ELuc (pox) and 2 μg of pNFκB-TK-SLR (nuc). One day after the transfection, the culture medium was replaced with DMEM without phenol red supplemented with 10 % FBS, 25 mM Hepes/NaOH (pH 7.0; Sigma-Aldrich), 200 μM D-luciferin potassium salt (Toyobo), and TNFα at 10 ng/ml. Bioluminescence was measured and calculated as reported previously [26]. Briefly, bioluminescence was recorded for 1 min at intervals of 10 min in the absence or presence of the R62 long-pass filter at 37 °C using an AB2500 Kronos (ATTO) dish-type luminometer. Bioluminescence intensity was expressed as counts per minute.

Results and discussion

Subcellular bioluminescence imaging using green-emitting ELuc and red-emitting SLR

The bioluminescent reporters used in this study were the green-emitting luciferase ELuc (λ_{max}=538 nm) from a Brazilian click beetle (*Pyrearinus termitilluminans*) [12, 35] and the red-emitting luciferase SLR (λ_{max}=630 nm) from a railroad worm (*Phrixothrix hirtus*) [18, 36] (Fig. 1). We chose these luciferases as reporters for the following reasons: (1) ELuc and SLR display the most blueshifted and redshifted spectra, respectively, among the beetle luciferases, which are most easily separable emissions; (2) these luciferases emit light with a single luciferin (D-luciferin), allowing simultaneous emission; and (3) the emission colors are not affected by intracellular pH changes [35, 36] and remain unchanged even with prolonged incubation in the cells [26]. To perform dual-color bioluminescence imaging at the subcellular level, ELuc was targeted to a peroxisome by utilizing its own peroxisomal targeting signal at the extreme C-terminus. SLR was targeted to a nucleus by fusing the nuclear localization signal from SV40 large T antigen at the C-terminus. To capture their emissions with a CCD camera, we chose the BG39 short-pass filter (maximum transmittance, 82 %; Fig. 1, dotted blue line) and the R62 long-pass filter (maximum transmittance, 92 %; Fig. 1, dotted purple line) for ELuc and SLR, respectively.

To determine whether subcellular bioluminescence imaging is possible using these luciferases as reporters, peroxisome-targeted ELuc and nuclear-targeted SLR were

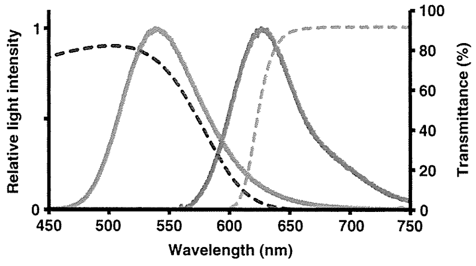

Fig. 1 Emission spectra of luciferases in viable cells and transmission spectra of the optical filters used in dual-color bioluminescence imaging. NIH3T3 cells were transfected with 2 μg of reporter plasmid pCMV-ELuc (pox) or pCMV-SLR (nuc), and the spectra were measured without destroying the cells. The bioluminescence spectra of peroxisome-targeted Emerald Luc (ELuc) and nuclear-targeted Stable Luciferase Red (SLR) are indicated by the *green line* and the *red line*, respectively. The transmission spectra of BG39 short-pass and R62 long-pass filters are shown by the *dotted blue line* and the *dotted purple line*, respectively

independently expressed in NIH3T3 cells under the control of the CMV promoter, and their images were captured using the ×40 objective lens without binning. As shown on the left in Fig. 2, peroxisome-localized ELuc exhibited a typical peroxisomal dot-like pattern, as reported previously [12]. The bioluminescence signal from nuclei was also clearly imaged using nuclear-targeted SLR (Fig. 2, right). We have previously demonstrated that bioluminescence imaging at the subcellular level with a high-magnification objective lens requires high signal intensity from living cells, and if the light intensity is insufficient, it would be difficult to acquire images at high temporal and/or spatial resolution, and this would result in low-resolution images [12]. We preliminarily estimated the light intensities of peroxisome-targeted ELuc and SLR from living cells to be 5×10^7 and 4×10^5 photons per second, respectively (data not shown), when measurements were conducted under the same conditions (same promoter and vector backbone) with a luminometer whose absolute responsivity was calibrated as reported previously [37]. Thus, although the light intensity of peroxisome-expressed SLR was approximately 1 % of that of peroxisome-expressed ELuc in living cells, we could acquire clear images of SLR in the nucleus (Fig. 2, right) by localizing SLR to the nucleus. Together, the results indicate that ELuc and SLR display sufficient light output intensity to make possible bioluminescence imaging of the peroxisome and the nucleus, respectively, in cells and that their emissions allow simultaneous imaging at subcellular resolution.

Next, we determined whether optical filters are appropriate to separate ELuc and SLR emissions. Peroxisome-targeted ELuc and nuclear-targeted SLR were expressed independently in NIH3T3 cells, and images were acquired in the absence or presence of optical filters. We obtained clear images of the peroxisome-localized ELuc luminescence with the BG39 short-pass filter (Fig. 3a, left), even though the light intensity was slightly lower (56.8±0.4 %) than that of the image taken in the absence of the filter, owing to emission loss caused by the filter. No remarkable luminescence signals were captured with the R62 long-pass filter (Fig. 3a and b, left). In contrast, clear images of the nuclear localization of SLR were obtained with the R62 long-pass filter, the light intensity of which was 62.5±1.5 % of that in the absence of the filter, but not with the BG39 short-pass filter (Fig. 3a and b, right). The results suggest that the BG39 and R62 filters are appropriate to capture the luminescence of ELuc and SLR, respectively, and that dual-color bioluminescence imaging at the subcellular level can be accomplished with these optical filters.

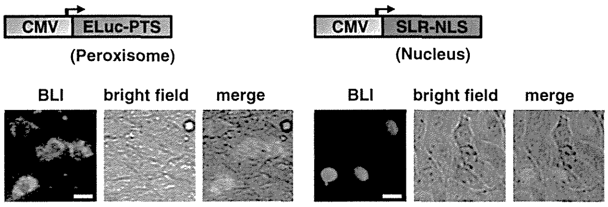

Fig. 2 Representative bioluminescence imaging of peroxisome-localized ELuc and nuclear-localized SLR in NIH3T3 cells. NIH3T3 cells were transfected independently with 2 μg of reporter plasmid pCMV-ELuc (pox) or pCMV-SLR (nuc). Luminescence images were acquired using 3-min exposure time and a ×40 objective lens without binning (*scale bar* 20 μm). A luminescence image, a bright-field photograph, and a merged photograph are shown in the panels on the *left*, in the *middle*, and on the *right*, respectively. Schematic drawings of the plasmids are shown at the *top*. *BLI* bioluminescence imaging. *CMV* cytomegalovirus promoter, *NLS* nuclear localization signal, *PTS* peroxisomal targeting signal

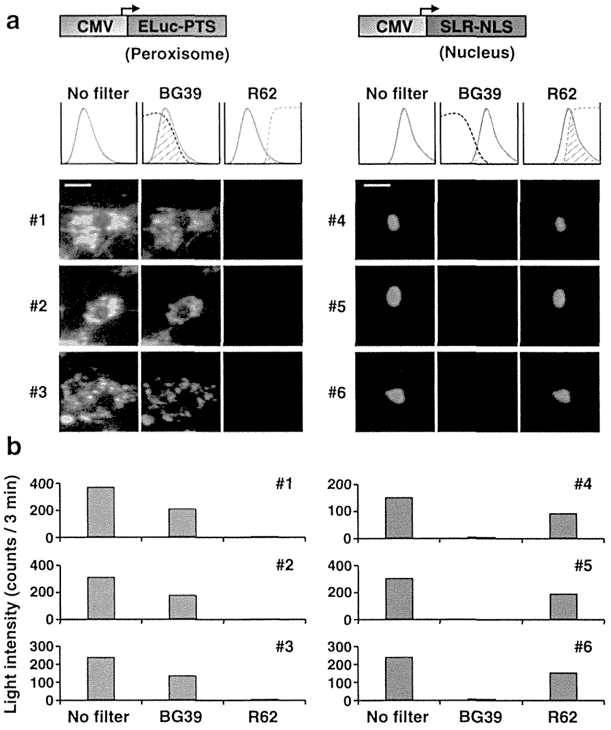

Fig. 3 Representative bioluminescence imaging of peroxisome-localized ELuc and nuclear-localized SLR in NIH3T3 cells using optical filters. **a** NIH3T3 cells were transfected independently with 2 μg of reporter plasmid pCMV-ELuc (pox) or pCMV-SLR (nuc). Luminescence images were acquired using 3-min exposure time and a ×40 objective lens without binning in the absence (indicated by *no filter*) or presence of BG39 and R62 filters (*scale bar* 20 μm). Schematic drawings of the plasmids are shown at the *top*. Schematic diagrams of the bioluminescence spectra of luciferases and the transmission spectra of the BG39 and R62 filters (*dotted lines*) are shown in the *middle*. Luminescence images of three representative cells with or without filters are shown at the *bottom*. **b** Quantified luminescence intensity of peroxisome-localized ELuc and nuclear-localized SLR shown in **a**

Dual-color bioluminescence imaging at the subcellular level

Next, we attempted to perform dual-color bioluminescence imaging. NIH3T3 cells were cotransfected with peroxisome-targeted ELuc and nuclear-targeted SLR, and images were taken using the ×40 objective lens in the presence of BG39 short-pass and R62 long-pass filters. One day after the transfection, ELuc emission through the BG39 filter and subsequent SLR emission through the R62 filter were captured in real time. Figure 4 shows representative images of three cells. As expected, we captured clearly and simultaneously ELuc luminescence from peroxisomes using the BG39 short-pass filter (Fig. 4, left) and SLR luminescence from nuclei using the R62 long-pass filter (Fig. 4, middle) even when these luciferases were co-expressed in a single cell. The merged photographs demonstrate that the respective luciferases are accurately localized to peroxisomes and nuclei in a cell (see also Movies S1, S2, S3). The results indicate that dual-color bioluminescence imaging at subcellular resolution can be performed using green-emitting ELuc and red-emitting SLR and the combined use of optical filters. Furthermore, time-lapse imaging demonstrated that the luminescence of peroxisome-localized ELuc and nuclear-localized SLR could be tracked continuously and simultaneously for a long time. These results appear to indicate that the dual-color bioluminescence imaging developed in this study makes possible quantitative imaging of gene expression changes in a single living cell at subcellular resolution.

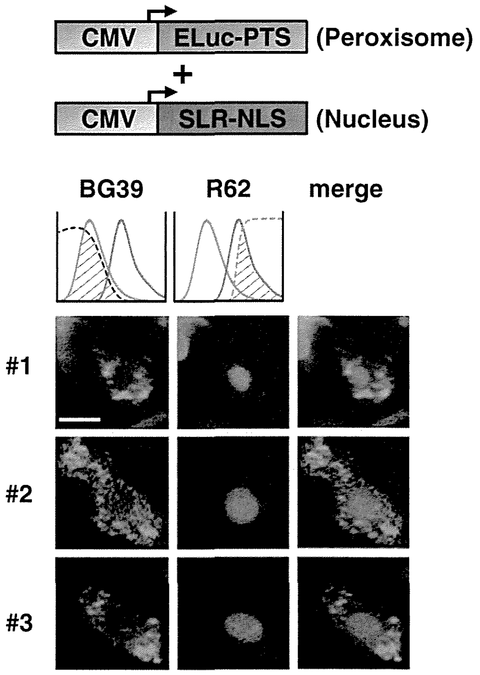

Fig. 4 Representative dual-color bioluminescence imaging of peroxisome-localized ELuc and nuclear-localized SLR in NIH3T3 cells. NIH3T3 cells were cotransfected with 1 μg of each reporter plasmid—pCMV-ELuc (pox) and pCMV-SLR (nuc)—and incubated for 1 day. Luminescence images were acquired using 3-min exposure time and a ×40 objective lens with BG39 and R62 filters (*scale bar* 20 μm). Images were taken without binning. Schematic drawings of the plasmids are shown at the *top*. Schematic diagrams of the bioluminescence spectra of the luciferases and the transmission spectra of the BG39 and R62 filters (*dotted lines*) are shown in the *middle*. Luminescence images acquired using the BG39 (green) and R62 (red) filters and merged images of three representative cells are shown at the *bottom*

Time-lapse dual-color imaging assay of NF-κB-dependent transactivation

To explore the possibility of quantitative imaging of the expressions of two genes by time-lapse dual-color imaging, we attempted to track the TNFα-induced activation of NF-κB, which is activated by cytokines, including TNFα, growth factors, and Toll-like receptor signaling [38, 39]. NF-κB exists in an inactive form in the cytoplasm owing to its interaction with IκB, an inhibitor of NF-κB. After activation of IκB kinase by TNFα, IκB is phosphorylated, ubiquitinated, and degraded by proteasomes. The dissociated NF-κB becomes free to translocate to the nucleus, where it activates specific target genes through selective binding to the NF-κB RE. Through such ways, NF-κB regulates the expression of a wide variety of genes, including cytokines, chemokines, and antiapoptotic genes [40].

For time-lapse dual-color bioluminescence imaging, we used nuclear-targeted SLR as the test reporter, whose expression is regulated by the NF-κB RE upstream of the thymidine kinase promoter. On the other hand, we used a reporter plasmid in which the peroxisome-targeted ELuc is expressed under the control of the CMV promoter, as the internal control reporter. NIH3T3 cells were cotransfected with these reporter plasmids. One day after the transfection, the medium was replaced with DMEM containing TNFα and D-luciferin. Time-lapse imaging was performed using the ×40 objective lens in the presence of BG39 and R62 filters, and images were captured for 3 min with 15-min intervals for 12 h. Figure 5a (see also Fig. S1a and Movies S4, S5, S6) shows representative images of SLR luminescence from the nucleus and ELuc luminescence from the peroxisomes of the TNFα-treated cells. After TNFα treatment, the intensity of the SLR signal that passed through the R62 long-pass filter gradually increased, whereas the intensity of the ELuc signal that passed through the BG39 filter slightly decreased or rapidly decayed after an abrupt increase, which might be due to cell death caused by TNFα stimulation. On the other hand, we could not detect distinct SLR signals from the nuclei of the TNFα-untreated cells even after 10 h, although ELuc luminescence from peroxisomes could be captured clearly (Fig. S1b). The results indicate that the increase in intensity of the SLR signal from the nucleus of TNFα-treated cells shown in Fig. 5a specifically monitors NF-κB RE-dependent transactivation via NF-κB activation pathways triggered by TNFα.

To estimate NF-κB RE-dependent transactivation, we quantified the SLR signals that passed through the R62 filter and the ELuc signals that passed through the BG39 filter (Fig. 5b, top), and the SLR signal intensity was normalized to the ELuc signal intensity, as analyzed by a typical dual-reporter assay (Fig. 5b, bottom). In two of three cells (cells 1 and 2), NF-κB RE-dependent transcription was initially rapidly activated but became constant after TNFα treatment for

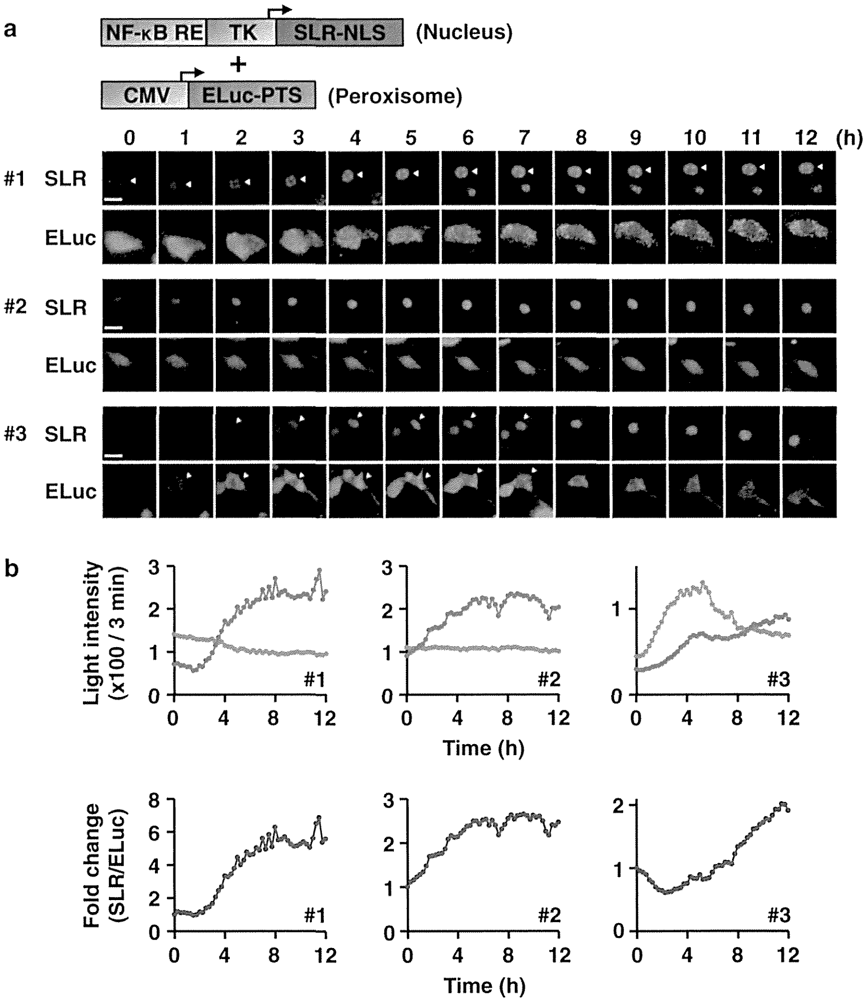

Fig. 5 Time-lapse dual-color bioluminescence imaging of tumor necrosis factor α (TNFα)-induced nuclear factor κB response element (NF-κB RE)-dependent transactivation in NIH3T3 cells. **a** NIH3T3 cells were cotransfected with 1 μg of reporter plasmid pCMV-ELuc (pox) and 2 μg of pNFκB-TK-SLR (nuc). One day after the transfection, the culture medium was replaced with Dulbecco's modified Eagle's medium supplemented with TNFα at 10 ng/ml. CCD images were acquired using 3-min exposure time at 15-min intervals for 12 h with a ×40 objective lens without binning (*scale bar* 20 μm). Representative serial luminescence images acquired using R62 (red, indicated as *SLR*) and BG39 (green, indicated as *ELuc*) filters at 1-h intervals are shown at the *bottom*. *White triangles* in the images indicate quantified organelle. Schematic drawings of the plasmids are shown at the *top*. **b** Recordings of ELuc (*green lines*) and SLR (*red lines*) luminescence shown in **a** (*top*), and fold change (*blue lines*), where the SLR intensity was normalized to the ELuc intensity (*bottom*). The fold change at time zero is set to 1. *TK* thymidine kinase promoter

8 h, whereas the NF-κB RE-dependent transcription of one cell (cell 3) was continuously activated. We assume that the differences in activation kinetics among the cells reflect differences in sensitivity to TNFα among the cells. We also confirmed the activation kinetics by means of real-time photomultiplier recording, in which the overall average of gene expressions was measured, under the same conditions as those for Fig. 5. After treatment with TNFα, the cells were acutely activated, and the bioluminescence intensity reached a maximum approximately 9 h after treatment and remained at this level until 12 h after treatment (Fig. S2), which was similar to the kinetics of cells 1 and 2. Thus, the kinetics of gene expression and activation measured by the two monitoring systems were very similar, suggesting the suitability of the bioluminescence imaging system developed in this work.

Thus, we have successfully used subcellular localized green-emitting ELuc and red-emitting SLR to visualize and quantify gene expression. This work is the first to demonstrate the time-lapse simultaneous imaging of the expressions of two genes by bioluminescence imaging at the subcellular level.

Conclusions

We have developed a dual-color bioluminescence imaging system in which peroxisome-targeted green-emitting ELuc and nuclear-targeted red-emitting SLR are used as reporters. This system allows us not only to track the subcellular localization of luciferases in a single cell with high spatial resolution, but also to analyze two gene expressions with high temporal resolution. The system offers several advantages for high spatiotemporal imaging for the continuous visualization of the intracellular localization of protein and gene expression at the subcellular level. This system can be easily used to analyze the intracellular trafficking of proteins, such as the nuclear entry of transcription factors, and the concomitant change of gene expression. Furthermore, the system can be also applied to subcellular imaging of intracellular dynamics of Ca^{2+} and ATP by combined use of aequorin, a blue-emitting Ca^{2+}-binding photoprotein, and SLR [41, 42], thereby making possible the simultaneous analysis of multiple cellular events.

Acknowledgments We thank T. Yamazaki from Toyobo for providing the NF-κB reporter vector. We also thank S. Kumata and M. Sasao from the National Institute of Advanced Industrial Science and Technology for excellent technical assistance. This study was supported by a Grant-in-Aid for Scientific Research (no. 21590266 to Y.N.) from the Japan Society for the Promotion of Science.

References

1. Naylor LH (1999) Reporter gene technology: the future looks bright. Biochem Pharmacol 58:749–757
2. Greer LF 3rd, Szalay AA (2002) Imaging of light emission from the expression of luciferases in living cells and organisms: a review. Luminescence 17:43–74
3. Gross S, Piwnica-Worms D (2005) Spying on cancer: molecular imaging *in vivo* with genetically encoded reporters. Cancer Cell 7: 5–15
4. Roda A, Guardigli M, Michelini E, Mirasoli M (2009) Bioluminescence in analytical chemistry and *in vivo* imaging. Trends Anal Chem 28:307–322
5. Nakajima Y, Ohmiya Y (2010) Bioluminescence assays: multicolor luciferase assay, secreted luciferase assay and imaging luciferase assay. Expert Opin Drug Discov 5:835–849
6. Welsh DK, Takahashi JS, Kay SA (2010) Suprachiasmatic nucleus: cell autonomy and network properties. Annu Rev Physiol 72: 551–577
7. Wilson T, Hastings JW (1998) Bioluminescence. Annu Rev Cell Dev Biol 14:197–230
8. Gandelman O, Allue I, Bowers K, Cobbold P (1994) Cytoplasmic factors that affect the intensity and stability of bioluminescence from firefly luciferase in living mammalian cells. J Biolumin Chemilumin 9:363–371
9. Ignowski JM, Schaffer DV (2004) Kinetic analysis and modeling of firefly luciferase as a quantitative reporter gene in live mammalian cells. Biotechnol Bioeng 86:827–834
10. Luker KE, Luker GD (2008) Applications of bioluminescence imaging to antiviral research and therapy: multiple luciferase enzymes and quantitation. Antiviral Res 78:179–187
11. Welsh DK, Kay SA (2005) Bioluminescence imaging in living organisms. Curr Opin Biotechnol 16:73–78
12. Nakajima Y, Yamazaki T, Nishii S, Noguchi T, Hoshino H, Niwa K, Viviani VR, Ohmiya Y (2010) Enhanced beetle luciferase for high-resolution bioluminescence imaging. PLoS One 5:e10011
13. Kitayama Y, Kondo T, Nakahira Y, Nishimura H, Ohmiya Y, Oyama T (2004) An *in vivo* dual-reporter system of cyanobacteria using two railroad-worm luciferases with different color emissions. Plant Cell Physiol 45:109–113
14. Cevenini L, Michelini E, D'Elia M, Guardigli M, Roda A (2013) Dual-color bioluminescent bioreporter for forensic analysis: evidence of androgenic and anti-androgenic activity of illicit drugs. Anal Bioanal Chem 405:1035–1045
15. Ogura R, Matsuo N, Wako N, Tanaka T, Ono S, Hiratsuka K (2005) Multi-color luciferase as reporters for monitoring transient gene expression in higher plants. Plant Biotechnol 22:151–155
16. Nakajima Y, Ikeda M, Kimura T, Honma S, Ohmiya Y, Honma K (2004) Bidirectional role of orphan nuclear receptor RORα in clock gene transcriptions demonstrated by a novel reporter assay system. FEBS Lett 565:122–126
17. Branchini BR, Southworth TL, Khattak NF, Michelini E, Roda A (2005) Red- and green-emitting firefly luciferase mutants for bioluminescent reporter applications. Anal Biochem 345:140–148
18. Nakajima Y, Kimura T, Sugata K, Enomoto T, Asakawa A, Kubota H, Ikeda M, Ohmiya Y (2005) Multicolor luciferase assay system: one-step monitoring of multiple gene expressions with a single substrate. Biotechniques 38:891–894
19. Branchini BR, Ablamsky DM, Murtiashaw MH, Uzasci L, Fraga H, Southworth TL (2007) Thermostable red and green light-producing firefly luciferase mutants for bioluminescent reporter applications. Anal Biochem 361:253–262
20. Davis RE, Zhang YQ, Southall N, Staudt LM, Austin CP, Inglese J, Auld DS (2007) A cell-based assay for IκBα stabilization using a two-color dual luciferase-based sensor. Assay Drug Dev Technol 5:85–103
21. Michelini E, Cevenini L, Mezzanotte L, Ablamsky D, Southworth T, Branchini B, Roda A (2008) Spectral-resolved gene technology for multiplexed bioluminescence and high-content screening. Anal Chem 80:260–267
22. Noguchi T, Ikeda M, Ohmiya Y, Nakajima Y (2008) Simultaneous monitoring of independent gene expression patterns in two types of cocultured fibroblasts with different color-emitting luciferases. BMC Biotechnol 8:40
23. Kafi AKM, Hattori M, Misawa N, Ozawa T (2011) Dual-color bioluminescence analysis for quantitatively monitoring G-protein-coupled receptor and β-arrestin interactions. Pharmaceuticals 4:457–469
24. Saito R, Hirakawa S, Ohara H, Yasuda M, Yamazaki T, Nishii S, Aiba S (2011) Nickel differentially regulates NFAT and NF-κB activation in T cell signaling. Toxicol Appl Pharmacol 254:245–255
25. Takahashi T, Kimura Y, Saito R, Nakajima Y, Ohmiya Y, Yamasaki K, Aiba S (2011) An *in vitro* test to screen skin sensitizers using a stable THP-1-derived IL-8 reporter cell line, THP-G8. Toxicol Sci 124:359–369
26. Noguchi T, Michihata T, Nakamura W, Takumi T, Shimizu R, Yamamoto M, Ikeda M, Ohmiya Y, Nakajima Y (2010) Dual-color luciferase mouse directly demonstrates coupled expression of two clock genes. Biochemistry 49:8053–8061
27. Noguchi T, Ikeda M, Ohmiya Y, Nakajima Y (2012) A dual-color luciferase assay system reveals circadian resetting of cultured fibroblasts by co-cultured adrenal glands. PLoS One 7:e37093
28. Naik S, Piwnica-Worms D (2007) Real-time imaging of β-catenin dynamics in cells and living mice. Proc Natl Acad Sci U S A 104: 17465–17470
29. Hida N, Awais M, Takeuchi M, Ueno N, Tashiro M, Takagi C, Singh T, Hayashi M, Ohmiya Y, Ozawa T (2009) High-sensitivity real-time imaging of dual protein-protein interactions in living subjects using multicolor luciferases. PLoS One 4:e5868
30. Mezzanotte L, Que I, Kaijzel E, Branchini B, Roda A, Lowik C (2011) Sensitive dual color *in vivo* bioluminescence imaging using a new red codon optimized firefly luciferase and a green click beetle luciferase. PLoS One 6:e19277
31. Mezzanotte L, Aswendt M, Tennstaedt A, Hoeben R, Hoehn M, Lowik C (2013) Evaluating reporter genes of different luciferases for optimized *in vivo* bioluminescence imaging of transplanted neural stem cells in the brain. Contrast Media Mol Imaging 8:505–513
32. Kwon H, Enomoto T, Shimogawara M, Yasuda K, Nakajima Y, Ohmiya Y (2010) Bioluminescence imaging of dual gene expression at the single-cell level. Biotechniques 48:460–462
33. Niwa Y, Shimojo H, Isomura A, Gonzalez A, Miyachi H, Kageyama R (2011) Different types of oscillations in Notch and Fgf signaling regulate the spatiotemporal periodicity of somitogenesis. Genes Dev 25:1115–1120
34. Imayoshi I, Isomura A, Harima Y, Kawaguchi K, Kori H, Miyachi H, Fujiwara T, Ishidate F, Kageyama R (2013) Oscillatory control of factors determining multipotency and fate in mouse neural progenitors. Science 342:1203–1208
35. Viviani VR, Silva AC, Perez GL, Santelli RV, Bechara EJ, Reinach FC (1999) Cloning and molecular characterization of the cDNA for the Brazilian larval click-beetle *Pyrearinus termitilluminans* luciferase. Photochem Photobiol 70:254–260
36. Viviani VR, Bechara EJ, Ohmiya Y (1999) Cloning, sequence analysis, and expression of active *Phrixothrix* railroad-worms luciferases:

relationship between bioluminescence spectra and primary structures. Biochemistry 38:8271–8279

37. Niwa K, Ichino Y, Ohmiya Y (2010) Quantum yield measurements of firefly bioluminescence reactions using a commercial luminometer. Chem Lett 39:291–293
38. Baker RG, Hayden MS, Ghosh S (2011) NF-κB, inflammation, and metabolic disease. Cell Metab 13:11–22
39. Tornatore L, Thotakura AK, Bennett J, Moretti M, Franzoso G (2012) The nuclear factor kappa B signaling pathway: integrating metabolism with inflammation. Trends Cell Biol 22:557–566
40. Ling J, Kumar R (2012) Crosstalk between NFκB and glucocorticoid signaling: a potential target of breast cancer therapy. Cancer Lett 322:119–126
41. Kwon HJ, Ohmiya Y, Honma KI, Honma S, Nagai T, Saito K, Yasuda K (2012) Synchronized ATP oscillations have a critical role in prechondrogenic condensation during chondrogenesis. Cell Death Dis 3:e278
42. Kwon HJ, Ohmiya Y, Yasuda K (2012) Dual-color system for simultaneously monitoring intracellular Ca^{2+} and ATP dynamics. Anal Biochem 430:45–47

Journal of Biotechnology 194 (2015) 115–123

Contents lists available at ScienceDirect

Journal of Biotechnology

journal homepage: www.elsevier.com/locate/jbiotec

Highly sensitive luciferase reporter assay using a potent destabilization sequence of calpain 3

Mayu Yasunaga[a], Kazutoshi Murotomi[a], Hiroko Abe[a], Tomomi Yamazaki[b], Shigeaki Nishii[b], Tetsuya Ohbayashi[c], Mitsuo Oshimura[d,e], Takako Noguchi[f], Kazuki Niwa[g], Yoshihiro Ohmiya[h], Yoshihiro Nakajima[a,*]

[a] *Health Research Institute, National Institute of Advanced Industrial Science and Technology (AIST), Takamatsu, Kagawa 761-0395, Japan*
[b] *Tsuruga Institute of Biotechnology, TOYOBO Corporation Ltd., Tsuruga, Fukui 914-0047, Japan*
[c] *Division of Functional Genomics, Research Center for Bioscience and Technology, Tottori University, Yonago, Tottori 683-8503, Japan*
[d] *Chromosome Engineering Research Center, Tottori University, Yonago, Tottori 683-8503, Japan*
[e] *Department of Biomedical Science, Institute of Regenerative Medicine and Biofunction, Graduate School of Medical Sciences, Tottori University, Yonago, Tottori 683-8503, Japan*
[f] *Department of Psychiatry and Center for Circadian Biology, University of California, San Diego, La Jolla, CA 92093-0603, USA*
[g] *National Metrology Institute of Japan (NMIJ), National Institute of Advanced Industrial Science and Technology (AIST), Tsukuba, Ibaraki 305-8063, Japan*
[h] *DAILAB, Biomedical Research Institute, National Institute of Advanced Industrial Science and Technology (AIST), Tsukuba, Ibaraki 305-8063, Japan*

ARTICLE INFO

Article history:
Received 13 July 2014
Received in revised form
18 November 2014
Accepted 10 December 2014
Available online 18 December 2014

Keywords:
Luciferase
Destabilization sequence
Calpain 3
Real-time monitoring

ABSTRACT

Reporter assays that use luciferases are widely employed for monitoring cellular events associated with gene expression in vitro and in vivo. To improve the response of the luciferase reporter to acute changes of gene expression, a destabilization sequence is frequently used to reduce the stability of luciferase protein in the cells, which results in an increase of sensitivity of the luciferase reporter assay. In this study, we identified a potent destabilization sequence (referred to as the C9 fragment) consisting of 42 amino acid residues from human calpain 3 (CAPN3). Whereas the half-life of Emerald Luc (ELuc) from the Brazilian click beetle *Pyrearinus termitilluminans* was reduced by fusing PEST ($t_{1/2} = 9.8$ to 2.8 h), the half-life of C9-fused ELuc was significantly shorter ($t_{1/2} = 1.0$ h) than that of PEST-fused ELuc when measurements were conducted at 37 °C. In addition, firefly luciferase (*luc2*) was also markedly destabilized by the C9 fragment compared with the humanized PEST sequence. These results indicate that the C9 fragment from CAPN3 is a much more potent destabilization sequence than the PEST sequence. Furthermore, real-time bioluminescence recording of the activation kinetics of nuclear factor-κB after transient treatment with tumor necrosis factor α revealed that the response of C9-fused ELuc is significantly greater than that of PEST-fused ELuc, demonstrating that the use of the C9 fragment realizes a luciferase reporter assay that has faster response speed compared with that provided by the PEST sequence.

1. Introduction

Reporter assay systems are widely used to study various biological functions, such as gene expression, post-translational modification, and protein–protein interaction, in vitro and in vivo (Greer and Szalay, 2002; Gross and Piwnica-Worms, 2005; Wilson and Hastings, 1998). Of the reporter genes known to date, luciferases that emit light by oxidizing their substrates are frequently employed because their sensitivity and range of linear response are superior to those of other typical reporters, including β-galactosidase, chloramphenicol acetyltransferase, and fluorescent proteins (Naylor, 1999). Thus, luciferases are the most suitable reporter genes for the quantitative measurement of cellular events, including gene expression.

In a typical luciferase reporter assay that uses firefly and *Renilla* luciferases, a luciferase-expressing object, such as a cell, is destroyed at a particular time point, called the endpoint assay, enabling conventional and high-throughput assay. On the other hand, *Gaussia*, *Metridia*, and *Cypridina* luciferases are secreted from cells by utilizing their own secretion signals, thereby allowing us to continuously monitor luciferase activity in the culture medium.

Abbreviations: CAPN3, calpain 3; ELuc, Emerald Luc from Brazilian click beetle *Pyrearinus termitilluminans*; CCD, charged-coupled device; *luc2*, firefly luciferase from *Photinus pyralis*; EGFP, enhanced green fluorescent protein; TK, thymidine kinase; NF-κB, nuclear factor-κB; TNFα, tumor necrosis factor α; MI-HAC, multi-integrase human artificial chromosome; DMEM, Dulbecco's Modified Eagle's Medium; FBS, fetal bovine serum; FISH, fluorescence in situ hybridization.

[*] Corresponding author. Tel.: +81 87 869 3525; fax: +81 87 869 4178.
E-mail address: y-nakajima@aist.go.jp (Y. Nakajima).

http://dx.doi.org/10.1016/j.jbiotec.2014.12.004
0168-1656/

Recent improvements of both the luciferases and the detection systems have enabled us to detect noninvasively bioluminescence from cells, tissues, and whole organisms in real time by using a photomultiplier tube or a highly sensitive charged-coupled device (CCD) camera (Luker and Luker, 2008; Nakajima and Ohmiya, 2010; Welsh and Kay, 2005). Such monitoring systems permit the kinetic analysis of gene expression and change of second messenger levels, such as ATP and Ca^{2+} (Grygorczyk et al., 2013; Kwon et al., 2012).

In general, bioluminescence detection sensitivity increases proportionally with the stability of luciferase protein in the cells due to the accumulation of residual luciferase protein. Conversely, it is known that a stable luciferase is inappropriate for the high-sensitivity detection of acute changes of cellular response, owing to the residual photonic contribution of the pre-existing luciferase protein (Leclerc et al., 2000). In this regard, for monitoring acute or transient changes of cellular response, a destabilization sequence is frequently used to reduce the stability of the luciferase protein in the cells. The most typical destabilization sequence is the PEST motif from the C-terminal region of ornithine decarboxylase. The PEST sequence, which consists of 41 amino acid residues, contains regions rich in proline, glutamate, serine, and threonine residues, and participates in proteolytic degradation (Rechsteiner and Rogers, 1996). By fusing the PEST sequence to the C-termini of luciferases, including firefly luciferase from *Photinus pyralis*, *Renilla* luciferase from *Renilla reinformis*, and Emerald Luc (ELuc) from *Pyrearinus termitilluminans*, the half-lives of those luciferases became significantly shorter than those of unmodified luciferases (Leclerc et al., 2000; Nakajima et al., 2010; Voon et al., 2005). Although the PEST sequence enables highly sensitive detection of rapid up- and downregulation of gene expression, a much more potent destabilization sequence is required to improve assay sensitivity. For this purpose, an mRNA degradation signal, such as an AU-rich element from an immediate early gene, such as c-fos or c-myc, is introduced into the 3′ untranslated region of the firefly and *Renilla* luciferase genes, in combination with the PEST sequence, to drastically destabilize mRNA and protein expression (Voon et al., 2005). However, the interpretation of the results of the luciferase assay would be more straightforward when the stability of luciferase protein is simply reduced by fusing the destabilization sequence only.

Calpain 3 (CAPN3, also called p94), a member of the calpain superfamily, is a calcium- or sodium-dependent cysteine protease mainly expressed in skeletal muscle, and is involved in many cellular functions, including cytoskeletal remodeling processes, cell differentiation, and apoptosis (Duguez et al., 2006; Sorimachi et al., 2011). CAPN3 is also known to be a short-lived protein. In vitro experiments demonstrated that CAPN3 was almost completely degraded within 10 min by autolysis (Fanin et al., 2007; Sorimachi et al., 1993). We therefore thought that a more rapid method for the destabilization of luciferase than the destabilization by PEST sequence could be achieved by fusing partial fragments of CAPN3 protein.

In this study, we identified a potent destabilization sequence consisting of 42 amino acid residues from CAPN3, which achieved more rapid degradation of luciferase in the cells than the PEST sequence. In addition, we successfully monitored the acute activation of nuclear factor-κB (NF-κB) by treatment with tumor necrosis factor α (TNFα), and confirmed that the sensitivity of the luciferase assay was markedly improved by using CAPN3-fused luciferase rather than PEST-fused luciferase.

2. Materials and methods

2.1. Plasmid construction

In the present study, the destabilization sequences were fused in-frame to the C-terminus of ELuc from *P. termitilluminans* (Nakajima et al., 2010). To construct an expression plasmid carrying cytosol-targeting ELuc, cDNA sequence in which the peroxisome-targeting signal (Ser-Lys-Leu) at the extreme C-terminus of ELuc was deleted by the polymerase chain reaction (PCR) with the pELuc-test (TOYOBO, Osaka, Japan) was used as the template, with the primer set SLGOR-T-F1 and ELuc(-PTS)-R-XbaI (Table S1). The amplified product was ligated into the *NcoI*/*XbaI* site of expression vector pGVC2 (TOYO Inc., Tokyo, Japan), from which the firefly luciferase was removed, resulting in pSV40-ELuc (cyto). PEST-fused ELuc, in which the PEST sequence is fused in-frame to the C-terminus of ELuc whose peroxisome-targeting signal has been removed, was prepared as reported previously (Nakajima et al., 2010). Briefly, the PEST sequence of mouse ornithine decarboxylase (in which the *NcoI* site at the C-terminal end was deleted without changing the deduced amino acid sequence) was PCR-amplified with pd1EGFP-N1 (Clontech, Palo Alto, CA) as the template using the primer set PEST-F-EcoRVm and PEST-R-XbaI, and the amplified product was ligated downstream of ELuc (cyto). The PEST-fused ELuc (cyto) was then replaced with the *NcoI* and *XbaI* fragment of pGVC2, from which the firefly luciferase was removed, resulting in pSV40-ELuc::PEST.

To generate an expression plasmid carrying CAPN3-fused ELuc, a partial sequence of human CAPN3 (hCAPN3) was PCR-amplified with FLJ40082 plasmid (TOYOBO) as the template using the primer set Capn3-F-SmaI and Capn3-R-XbaI, and the amplified product was ligated into the *EcoRV*/*XbaI* site of pSV40-ELuc::PEST, from which the PEST sequence was removed, resulting in pSV40-ELuc::CAPN3. Expression plasmids carrying CAPN3 fragments N1-, C1-, C2-, and C3-fused ELuc were prepared by inverse PCR using a KOD -Plus- Mutagenesis Kit (TOYOBO) with pSV40-ELuc::CAPN3 as the template, and primer sets Capn3-R1 and SV40-pA-F (for the N1 fragment), ELuc(-PTS,-Stop)-R-EcoRV and Capn3-F1 (for the C1 fragment), ELuc(-PTS,-Stop)-R-EcoRV and Capn3-F2 (for the C2 fragment), and Capn3-R2 and SV40-pA-F (for the C3 fragment), respectively, resulting in pSV40-ELuc::CAPN3-N1, pSV40-ELuc::CAPN3-C1, pSV40-ELuc::CAPN3-C2, and pSV40-ELuc::CAPN3-C3. The C4 to C9 fragments of CAPN3 were amplified by PCR with the FLJ40082 plasmid as the template using primer sets Capn3-F1 and Capn3-R3-XbaI (for the C4 fragment), Capn3-F4 and V-R4-XbaI (for the C5 fragment), Capn3-F5 and Capn3-R5-XbaI (for the C6 fragment), Capn3-F2 and Capn3-R6-XbaI (for the C7 fragment), Capn3-F6 and Capn3-R7-XbaI (for the C8 fragment), and Capn3-F7 and Capn3-R-XbaI (for the C9 fragment), respectively. The amplified fragments were digested with *XbaI* and ligated into the *EcoRV*/*XbaI* site of pSV40-ELuc::PEST, from which the PEST sequence was removed, resulting in pSV40-ELuc::CAPN3-C3, pSV40-ELuc::CAPN3-C4, pSV40-ELuc::CAPN3-C5, pSV40-ELuc::CAPN3-C6, pSV40-ELuc::CAPN3-C7, pSV40-ELuc::CAPN3-C8, and pSV40-ELuc::CAPN3-C9. The C10, C11, and C12 fragments of CAPN3 were prepared by annealing the following sets of 5′-phosphorylated oligonucleotides: Capn3-C10F and Capn3-C10R (for the C10 fragment), Capn3-C11F and Capn3-C11R (for the C11 fragment), and Capn3-C12F and Capn3-C12R (for the C12 fragment), respectively. Phosphorylated double-strand DNAs were ligated into pSV40-ELuc::CAPN3, from which the CAPN3 sequence was removed by inverse PCR using the primer set ELuc(-PTS,-Stop)-R-EcoRV and SV40-pA-F, resulting in pSV40-ELuc::CAPN3-C10, pSV40-ELuc::CAPN3-C11, and pSV40-ELuc::CAPN3-C12.

To generate an expression plasmid carrying humanized PEST (hPEST)-fused firefly luciferase (*luc2*), hPEST-fused *luc2* was excised with *NcoI* and *XbaI* from pGL4.37 (Promega, Madison, WI), and the fragment was ligated into the *NcoI*/*XbaI* site of pSV40-ELuc::CAPN3-C9 from which ELuc::CAPN3-C9 fragment was removed, resulting in pSV40-luc2::hPEST. An expression plasmid carrying CAPN3-C9-fused *luc2* was generated by using the In

Fusion System (Clontech). First, the CAPN3-C9 fragment was PCR-amplified with pSV40-ELuc::CAPN3-C9 as the template using the primer set Capn3-13F-luc2-EcoRV and Capn3-13R-pGVC2. Next, *luc2* cDNA without the hPEST sequence was PCR-amplified with pGL4.37 as the template using the primer set luc2-F-pGVC2-HindIII and luc2-R-Capn3c9-EcoRV. The amplified products were simultaneously ligated into the *Hind*III/*Xba*I site of pSV40-ELuc::CAPN3-C9 from which the ELuc::CAPN3-C9 fragment was removed, using the In Fusion System according to the manufacturer's instructions, resulting in pSV40-luc2::CAPN3-C9.

To generate an expression plasmid carrying C9-fused enhanced green fluorescent protein (EGFP), the CAPN3-C9 fragment was PCR-amplified with pSV40-ELuc::CAPN3-C9 as the template using the primer set Capn3-F7 and Capn3-R-XbaI, and the fragment was ligated into the *Sma*I/*Xba*I site of pEGFP-C2 (Clontech) downstream of EGFP, resulting in pCMV-EGFP::CAPN3-C9.

To generate NF-κB reporter plasmids, oligonucleotides containing six tandem repeats of the NF-κB response element (5′-CGGAAAGTCCCA-3′) were ligated into the *Xho*I/*Bgl*II site of pSLR-HSVtk Control (TOYOBO), immediately upstream of the herpes simplex virus thymidine kinase (TK) promoter. The SLR gene was replaced with *Nco*I and *Xba*I fragment of pSV40-ELuc (cyto), pSV40-ELuc::PEST, and pSV40-ELuc::CAPN3-C9. Then, expression cassettes consisting of the NF-κB response element, the HSV-TK promoter, ELuc or destabilized ELuc, and polyA signal were amplified by PCR using the primer set SLGOR-T-F2 and SLGOR-T-R1, and the amplified products were cloned into pENTR-D-TOPO (Invitrogen). The expression cassettes were recombined into pNeo-φC31 attB (Yamaguchi et al., 2011) by the LR reaction using LR Clonase II Plus Enzyme Mix (Invitrogen), yielding pφC31-Neo-NFκB-ELuc, pφC31-Neo-NFκB-ELuc::PEST, and pφC31-Neo-NFκB-ELuc::CAPN3-C9.

2.2. Cell culture

Mouse NIH3T3 cells (Riken Cell Bank 1862) and A9 cells harboring the multi-integrase human artificial chromosome (MI-HAC) vector (Yamaguchi et al., 2011) were grown in Dulbecco's Modified Eagle's Medium (DMEM, Sigma–Aldrich, St. Louis, MO) supplemented with 10% fetal bovine serum (FBS, ICN Biochemicals, Aurora, OH) in a humidified atmosphere containing 5% CO_2 at 37 °C.

2.3. Measurement of stability of luciferases in NIH3T3 cells

NIH3T3 cells were seeded in 96-well black clear-bottom plates (Nunc, Wiesbaden, Germany) at 2×10^4 cells per well one day before transfection. One hundred nanograms of reporter plasmid was transfected using Lipofectamine PLUS (Invitrogen) according to the manufacturer's instructions. One day after transfection, the culture medium was replaced with DMEM without phenol red (Gibco-BRL, Grand Island, NY) but supplemented with 10% FBS, 200 μM D-luciferin potassium salt (TOYOBO) that had been dissolved in distilled water, and 100 μM cycloheximide (Nacalai Tesque), and overlaid with 50 μl of mineral oil (Sigma–Aldrich) to prevent evaporation. Bioluminescence was recorded in real time for 10 s at 10-min intervals for 9.6 h at 37 °C using a microplate-type luminometer (AB-2350 Phelios, ATTO, Tokyo, Japan) unless otherwise noted.

2.4. Immunoblot analysis

NIH3T3 cells were seeded in six-well plates at the density of 5×10^5 cells per well one day before transfection. Two micrograms of expression plasmid was transfected into the cells, and the cells were incubated for two days. Thereafter, the culture medium was replaced with DMEM supplemented with 10% FBS and 100 μM cycloheximide. The cells were incubated at 37 °C under 5% CO_2 atmosphere, and lysed with M-PER extraction reagent (Pierce Biotechnology, Rockford, IL) supplemented with protease inhibitor cocktail (Roche, Basel, Switzerland). For the detection of ELuc and EGFP, we used rabbit anti-ELuc and anti-EGFP polyclonal antibodies that were raised against purified recombinant ELuc (Nakajima et al., 2010) and EGFP. For the detection of tubulin, mouse anti-α-tubulin (Sigma–Aldrich) was used as the primary antibody. We used horseradish peroxidase-conjugated anti-rabbit IgG (Jackson ImmunoResearch, West Grove, PA) and anti-mouse IgG (BioRad, Hercules, CA) as the secondary antibodies. The antibodies were diluted with Can Get Signal solution (TOYOBO) (1/20,000, 1/20,000, and 1/3,000 dilution for anti-ELuc, anti-EGFP, and anti-tubulin antibodies, respectively). Immunoreactive bands were detected with the ECL Plus kit (GE Healthcare, Freiburg, Germany) according to the manufacturer's instructions using an image analyzer (LAS-3000 mini, Fuji Photo Film, Tokyo, Japan).

2.5. Generation of stable cell lines

Mouse fibroblast A9 cells harboring the MI-HAC vector were seeded in six-well plates at 6×10^5 cells per well one day before transfection. Three micrograms of reporter plasmid, pφC31-Neo-NFκB-ELuc, pφC31-Neo-NFκB-ELuc::PEST or pφC31-Neo-NFκB-ELuc::CAPN3-C9, was co-transfected with 1 μg of φC31 recombinase expression plasmid pCMV-φC31 (Yamaguchi et al., 2011) using Lipofectamine PLUS (Invitrogen) according to the manufacturer's instructions. The transfected cells were seeded in 10-cm dishes one day after transfection, and subcultured for selection with 800 μg/ml G418 (Nacalai Tesque). Integration of transgene into the corresponding site on the HAC vector was confirmed by genomic PCR using the primer set PGK5 and G418 3AS.

2.6. Fluorescence in situ hybridization (FISH) analysis

Preparation of metaphase chromosome from exponentially growing cell culture and FISH were performed as reported previously (Tomizuka et al., 1997). Briefly, FISH was carried out using digoxigenin-labeled (Roche, Basel, Switzerland) human COT1 DNA (Invitrogen) and biotin-labeled reporter plasmid pφC31-Neo-NFκB-ELuc. Chromosome DNA was counterstained with DAPI (Sigma–Aldrich). Images were captured with a fluorescence microscope BX51 (Olympus, Tokyo, Japan).

2.7. Real-time bioluminescence measurement of TNFα-induced NF-κB activation

The A9 stable cell lines in which the NF-κB reporter plasmid was integrated into the MI-HAC vector were seeded in 35-mm dishes at 6×10^5 cells per dish. After one day, the medium was replaced with DMEM without phenol red (Gibco-BRL) and supplemented with 10% FBS and 10 ng/ml TNFα (Wako, Tokyo, Japan), and incubated for 15 min. The medium was again replaced with DMEM without phenol red (Gibco-BRL) but containing 10% FBS and 200 μM D-luciferin potassium salt (TOYOBO) that had been dissolved in distilled water, and overlaid with mineral oil (Sigma–Aldrich) to prevent evaporation. Bioluminescence was recorded for 1 min at 15-min intervals under a 5% CO_2 atmosphere at 37 °C using a dish-type luminometer (AB2500 Kronos, ATTO).

2.8. Time-lapse bioluminescence imaging

The A9 stable cell lines in which the NF-κB-ELuc::CAPN3-C9 reporter plasmid was integrated into the MI-HAC vector were seeded in 35-mm glass-bottom dishes (Iwaki, Tokyo, Japan) at 6×10^5 cells per dish. After one day, the medium was replaced with

DMEM without phenol red (Gibco-BRL) but supplemented with 10% FBS, 25 mM Hepes/NaOH (pH 7.0; Sigma–Aldrich), 500 μM D-luciferin potassium salt (TOYOBO) that had been dissolved in distilled water, and 10 ng/ml TNFα (Wako), and was sealed with Parafilm (American National Can, Menasha, IL) to prevent evaporation. Bioluminescence imaging was performed using the luminescence microscope CellGraph (ATTO) at 37 °C. CCD images were acquired with a 10-min exposure time at 15-min intervals with a 4× objective lens (NA, 0.5; ATTO) at 1 × 1 binning of the 512 pixel × 512 pixel array. Luminescence intensity was quantified with CellGraph Viewer (ATTO) and Metamorph (Universal Imaging, Brandywine, PA).

3. Results

3.1. *CAPN3 significantly destabilizes luciferase protein in cells more than PEST sequence*

In this study, we used the FLJ40082 clone (GenBank accession number AK097401) as hCAPN3 cDNA, which is a close homologue, and the partial sequence of the entire hCAPN3 (GenBank accession number AF209502), which corresponded to amino acid residues between 104 and 513 of hCAPN3 (Fig. S1, hereinafter referred to as CAPN3), and ELuc (Nakajima et al., 2010) as reporter. As ELuc exhibits brighter luminescence in cells compared with other beetle luciferases, including the firefly luciferase, because of the high stability of ELuc in the cells, it allowed us to reliably estimate the destabilization effect of CAPN3. The functional half-life of destabilized ELuc was estimated as the half-decay time of the luminescence intensity recorded over time in the presence of the protein synthesis inhibitor cycloheximide.

To determine whether the stability of ELuc can be reduced by CAPN3, CAPN3 cDNA was fused in-frame to the C-terminus of ELuc (Fig. S2). As shown in Fig. 1, whereas the functional half-life of unmodified ELuc in NIH3T3 cells was 9.83 h under the experimental conditions used in this study, the half-life of CAPN3-fused ELuc was significantly shortened (1.72 h). Furthermore, the half-life of CAPN3-fused ELuc was shorter than that of ELuc fused to the typical destabilizing motif PEST sequence from mouse ornithine decarboxylase (2.80 h), suggesting that CAPN3 contains a very effective destabilizing motif.

Western blot analysis using anti-ELuc antibody revealed that the amount of residual CAPN3-fused ELuc protein in the cells at time 0 was much smaller than that of the unmodified ELuc and the PEST-fused ELuc, and that the CAPN3-fused ELuc protein was rapidly degraded during incubation in the presence of cycloheximide (Fig. 1b). The results indicate that the decay of bioluminescence kinetics and light intensity caused by fusing CAPN3 is due not to the inhibition of the luciferin-luciferase reaction, but to the degradation of ELuc protein in the cells.

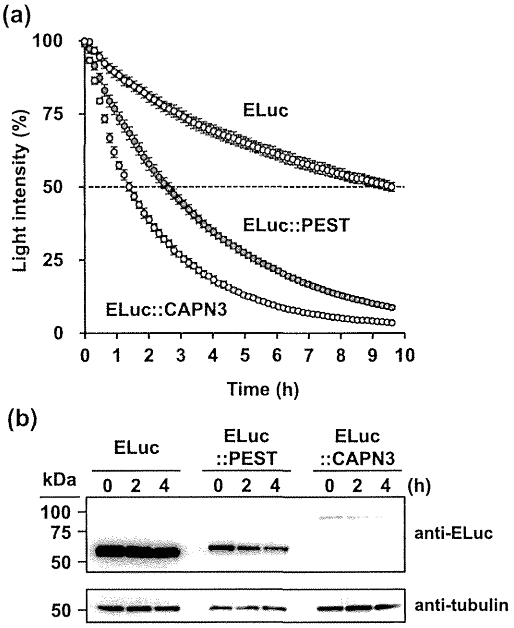

Fig. 1. Stability of ELuc, PEST-fused ELuc, and CAPN3-fused ELuc in NIH3T3 cells. (a) Functional half-lives of ELuc, PEST-fused ELuc, and CAPN3-fused ELuc. Expression plasmids pSV40-ELuc (cyto), pSV40-ELuc (cyto)::PEST, and pSV40-ELuc (cyto)::CAPN3 were independently transfected into NIH3T3 cells seeded in 96-well plates. One day after transfection, the culture medium was replaced with DMEM supplemented with 10% FBS, 200 μM D-luciferin, and 100 μM cycloheximide. Bioluminescence was recorded in real time for 10 s at 10-min intervals for 9.6 h at 37 °C. The maximum peak values were set to 100%. Error bars indicate the standard deviation ($n = 4$). (b) Western blot analysis of unmodified ELuc, PEST-fused ELuc, and CAPN3-fused ELuc in NIH3T3 cells. The expression plasmids were transfected into NIH3T3 cells, and incubation was carried out for two days. The culture medium was replaced with DMEM supplemented with 10% FBS and 100 μM cycloheximide, and incubation was carried out for 0, 2, and 4 h. Luciferase was detected using the anti-ELuc antibody. Tubulin was used as the internal control. The positions of molecular weight markers are indicated on the left of each panel.

3.2. *Identification of minimum destabilization sequence in CAPN3*

We identified the minimum CAPN3 sequence that can effectively destabilize luciferase protein in the cells, as the minimum fragment size would reduce the risk of loss of luciferase activity due to interference with the active conformation and/or the luciferin-luciferase reaction when the fragment is fused to luciferase. First, CAPN3 was divided into two fragments (N1 and C1 fragments), and the half-lives and the light intensities of ELuc fused at C-terminus to those fragments in the NIH3T3 cells were determined by real-time bioluminescence measurements (Figs. 2, S3, and S4). We examined the stability and the light intensity of ELuc fused to CAPN3 fragments using a 96-well plate format, which enables a direct comparison to a control experiment with PEST sequence performed in parallel. Both the half-life and the light intensity of N1-fused ELuc were severely reduced (0.57 h and 1.6% of PEST-fused ELuc (light intensity of PEST-fused ELuc was set to 100%), respectively), making it inappropriate for use in the reporter gene assay due to insufficient light output. We therefore chose the C1 fragment (half-life and light intensity were 1.83 h and 37.0%, respectively) to optimize the minimum sequence. The C1 fragment was further divided into two fragments (C2 and C3). The half-life of C3-fused ELuc was shorter (1.18 h) than that of C2-fused ELuc (2.55 h). Although the C2 fragment was further divided into three fragments (C4, C5, and C6), the half-lives of ELuc fused to those fragments were longer than that of C2-fused ELuc, indicating that an effective destabilization sequence does not exist in the C2 fragment and the sequence is included in the C3 fragment. Next, the C3 fragment was divided into three fragments (C7, C8, and C9 fragments). The half-lives of ELuc fused to the C7 and C8 fragments were longer (6.10 and 7.83 h for C7 and C8 fragments, respectively), whereas that of C9-fused ELuc was slightly shorter (0.99 h) than the half-life of the original C3-fused ELuc. To minimize the amino acid sequence of the C9 fragment (42 amino acid residues, Figs. 2b and S3), the C9 fragment was further divided into two fragments (C10 and C11), but the half-lives of ELuc fused to those fragments were longer than that of C9-fused ELuc. Finally, we made the C12 fragment by deleting the N-terminal ten residues of C9, but the half-life of C12-fused ELuc was also longer. Correlations between the half-lives and the light intensities indicate that the total amount of ELuc protein existing in cells is affected by the half-lives (Fig. S5).

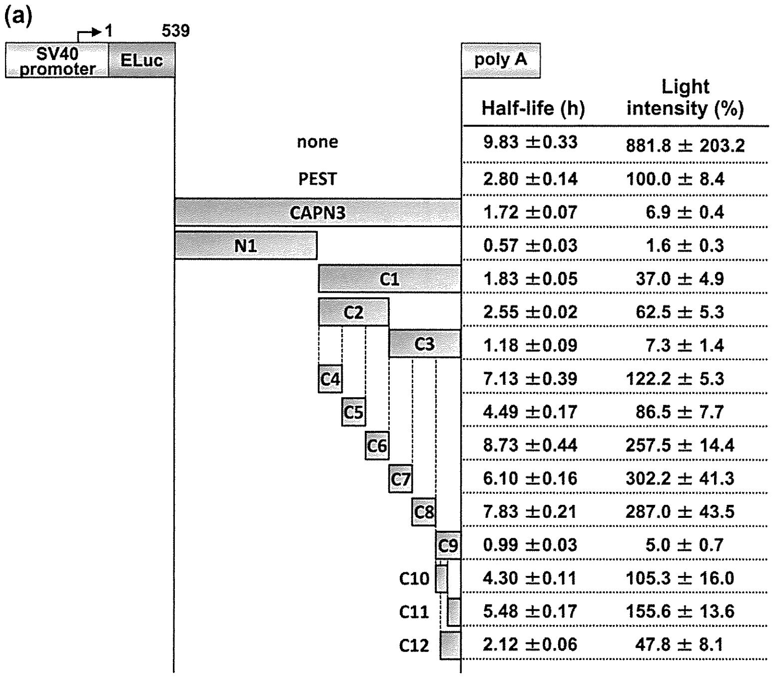

	Half-life (h)	Light intensity (%)
none	9.83 ±0.33	881.8 ± 203.2
PEST	2.80 ±0.14	100.0 ± 8.4
CAPN3	1.72 ±0.07	6.9 ± 0.4
N1	0.57 ±0.03	1.6 ± 0.3
C1	1.83 ±0.05	37.0 ± 4.9
C2	2.55 ±0.02	62.5 ± 5.3
C3	1.18 ±0.09	7.3 ± 1.4
C4	7.13 ±0.39	122.2 ± 5.3
C5	4.49 ±0.17	86.5 ± 7.7
C6	8.73 ±0.44	257.5 ± 14.4
C7	6.10 ±0.16	302.2 ± 41.3
C8	7.83 ±0.21	287.0 ± 43.5
C9	0.99 ±0.03	5.0 ± 0.7
C10	4.30 ±0.11	105.3 ± 16.0
C11	5.48 ±0.17	155.6 ± 13.6
C12	2.12 ±0.06	47.8 ± 8.1

(b)

```
C9 : -DDSEVICSFLVALMQKNRRKDRKLGASLFTIGFAIYEVPKEV-
C10: -DDSEVICSFLVALMQKNRRK----------------------
C11: --------------------DRKLGASLFTIGFAIYEVPKEV-
C12: -----------VALMQKNRRKDRKLGASLFTIGFAIYEVPKEV-
```

Fig. 2. Half-lives and light intensities of ELuc destabilized by fusing CAPN3 fragments. (a) Half-lives and light intensities of CAPN3-fused ELuc. Transfection and bioluminescence measurements were performed as described in the legend of Fig. 1 (see also Section 2). Light intensity was calculated from the integrated values of each count, and the light intensity of PEST-fused ELuc of that was set to 100%. Values are expressed as means ± standard deviation ($n = 4$). Schematic representation of expression plasmids is shown on the left. CAPN3 and its fragments are shown between ELuc and polyA, where N and C indicate N- and C-termini, respectively, and digits indicate fragment number. (b) Deduced amino acid sequences of C9, C10, C11, and C12 fragments of CAPN3.

To confirm whether the rapid reduction of the light intensity of ELuc by fusion to the C9 fragment was accompanied by the degradation of the ELuc protein in the cells, we performed western blot analysis using anti-ELuc. As shown in Fig. 3a, the immunoreactive bands corresponding to C9-fused ELuc became thinner over time after the cells were treated with cycloheximide (left panel), and its degradation kinetics (right panel) was similar to the luminescence decay kinetics (Fig. 3b), indicating that the ELuc protein was destabilized by fusion to the C9 fragment. We decided, therefore, that the C9 fragment, which consists of 42 amino acid residues corresponding to the amino acid residues from 472 to 512 of hCAPN3 (GenBank accession number AF209502), except for valine at the extreme C-terminus of C9 (Fig. S1), is the minimum destabilization sequence, and used it in the following experiments.

3.3. Destabilization of firefly luciferase and green fluorescent protein by C9 fragment

To confirm whether the C9 fragment identified as the minimum destabilization sequence of CAPN3 could destabilize other reporter proteins in the cells, we fused the C9 fragment to the C-terminus of firefly luciferase (*luc2*), the most popular luciferase reporter gene, and EGFP. First, we compared the functional half-lives of hPEST-fused and C9-fused *luc2* in NIH3T3 cells. An expression plasmid was transfected into NIH3T3 cells, and bioluminescence intensity was measured in real time in the presence of cycloheximide. As shown in Fig. 4a, the half-life of C9-fused *luc2* (0.18 h) was markedly short compared with that of hPEST-fused *luc2* (1.62 h).

Next, we examined the stability of unmodified and C9-fused EGFP in NIH3T3 cells. An expression plasmid was transfected into the cells, and the cells were incubated in the presence of cycloheximide for 4 h. EGFP protein levels were analyzed by western blotting using anti-EGFP antibody. As shown in Fig. 4b, whereas the immunoreactive bands corresponding to unmodified EGFP showed no changes, the bands corresponding to C9-fused EGFP became thinner over time after the cells were treated with cycloheximide. In addition, the amount of residual C9-fused EGFP protein in the cells at time 0 was much smaller than that of the unmodified EGFP, indicating that EGFP can be significantly destabilized by fusing the C9 fragment in the cells. The results together suggest that C9 fragment identified in this study can destabilize not only luciferase proteins but also other reporter proteins, including fluorescent proteins.

3.4. C9 fragment of CAPN3 improves sensitivity of luciferase assay for acute gene expression

To examine whether the C9 fragment of CAPN3 can monitor acute gene expression more sensitively than the PEST sequence when fused to ELuc, we examined the TNFα-induced transactivation of NF-κB, a transcription factor involved in the regulation of inflammation, immune response, and apoptosis (Tornatore et al., 2012), by means of real-time bioluminescence measurements